Multiviewing/Multispectral POLDER aerosol optical properties retrieval using SCIATRAN: Global validation

Master Thesis

Institute of Environmental Physics

Bremen, December, 2021

Author:	Khalid El Maghawry Elsayed
Matriculation:	3128607
Degree program:	M.Sc. Environmental Physics
Supervisors:	Prof. Dr. John P. Burrows
	Dr. Marco Vountas

Contents

1 Introduction

Aerosols are tiny suspended particles (liquid or solid) in the atmosphere. The aerosols can be categorized based on which part of the atmosphere they reside. Aerosols can have natural or human-made origin. About 90% of aerosol mass has natural origins as dust from deserts, ashes from volcanoes, or sea salt from oceans while 10% is anthropogenic. Anthropogenic aerosol is generated by fossil fuel combustion, biomass burning, and industrial activities in general. The terrestrial aerosols have significant implications on the air quality affecting public health. Additionally they can reduce the visibility, impacting aviation security [2]. Aerosols are capable of backscattering and absorbing solar radiation, strongly influencing the Earth's energy budget. Consequently, they have direct impact on the climate in addition to large uncertainty in future climate prediction due to cloud-aerosol interaction [2].

Aerosol's range of influence is attributable to various characteristics such as particle size distribution, optical properties, and chemical composition. The aerosols are often composed of sulfates, organic carbon, black carbon, nitrates, mineral dust, sea salt and others. But in fact, these groups do not provide an accurate description as aerosols interact with each other and create complex mixtures. The other important parameter is the particle size which is often divided into three modes: Aitken (< 0.2 μm), Large (0.2-2 μm), and Giant (>2 μm).

The increase of aerosol concentration often influences the planet by cooling the atmosphere but it also has the potential to warm the surrounding. It cools the atmosphere directly by reflecting, scattering, or absorbing the incoming solar radiation. This decreases the radiation reaching the Earth's surface or indirectly by entering the clouds and acting as cloud condensation nuclei, causing the droplets to increase in number and decrease in size. The net effect is that clouds reflect more sunlight and have longer lifetime in the atmosphere affecting precipitation patterns. Furthermore, aerosols and cloud droplets absorb part of the beam decreasing the solar radiation reaching the earth's surface. To accentuate the role aerosols play in the atmosphere, detailed studies of their physical properties and chemical composition are carried out.

The Aerosol Optical Thickness (AOT) or Aerosol Optical Depth (AOD) is considered as a fundamental parameter to investigate aerosols. AOD and AOT are considered synonymous in most of the scientific literature related to the terrestrial atmosphere and the term AOT will be used in this study. AOT is a quantitative estimate of the amount of aerosol present in the atmosphere. It is an indicator of the level to which aerosols disrupt solar radiation transmission in the atmosphere by scattering, absorption, or reflection. Mathematically, it is the integral of the aerosol extinction coefficient vertically along the atmospheric column. Several instruments and methods were developed to measure AOT directly and indirectly.

These provide different types of data: (1) point data from ground-based stations (high accuracy) (2) space observations by satellites (lower accuracy), and other. The load and type of aerosol change rapidly over time and location. Accordingly, satellite measurements have become valuable. These provide high spatial and temporal resolution allowing investigations with wider spatial coverage, often sufficient temporal variation, and vertical distribution on a local and global scale with moderate data quality. Multi-wavelength sun-photometric measurements are considered as the most accurate source of AOT data [49]. Thus, these kind of ground-based measurements are more reliable and they can be used to validate the AOT retrievals from satellite observations. The development of AOT retrieval algorithms from satellite measurements become more needed in the society of atmospheric sciences.

This study is an extension of a previous work of Vountas et al.(2020). The preceding work has presented a novel approach to retrieve AOT and surface reflectance. The retrieval was based on multi-spectral and multi-viewing space-borne measurements from Polarization and Directionality of Earth's Reflectances-3 (POLDER) instrument, and is using the radiative transfer and retrieval model SCIATRAN. The model is utilizing an analytical linearized retrieval mode and Ross-Li model to parametrize the surface[2]. The retrieval algorithm was validated using Atmospheric Radiation Measurement Climate Research Facilities (ARM) in the Southern Great Plains (SGP, USA). The validation was done by comparing the retrieved AOT values with ground-based measurements of ARM. In this former study, the validation was limited to only two scenes (on two days of POLDER measurements).

The present study, in this thesis, aims at providing a significantly larger database by retrieving one month of POLDER data using SCIATRAN and performing a global validation to achieve a better understanding of the quality of the retrieval. As the retrieval in its current form is very time consuming[1], retrievals are only performed over locations providing validation information. The extended validation was done using AERONET (AErosol RObotic NETwork) dataset. AERONET is a global network of ground-based remote sensing stations founded by The National Aeronautics and Space Administration (NASA) and Le Centre National de la Recherche Scientifique (CNRS). Its data base is expanded by collaboration with other research institutes, universities, and agencies. The AERONET stations are provided with a sun photometer that measures spectral sun irradiance and sky radiances, which are used to retrieve a long-term database of optical, microphysical and radiative properties for aerosol research and characterization or validation of satellite retrievals.

[1] 30-50 groundpixels of POLDER data consume 30 min. of net run time on state-of-the-art high performance computing cluster.

The thesis work starts by reviewing the past literature and the scientific background of the topic in chapter 2. Chapter 3 is describing the utilized datasets in the study. The radiative transfer model SCIATRAN, described in chapter 4, has been run to retrieve the extracted POLDER data using the same parameter settings utilized in Vountas et al. (2020). In this study, POLDER level-1 data have been processed and co-located with observations of AERONET stations using a recently developed python tool described in detail in chapter 5. A detailed evaluation of the retrieval algorithm output has been done based on a systematic evaluation scheme is given in chapter 5.2. The results of the retrieval and validation are displayed and discussed in chapter 6. The study is concluded and the outlook and recommendations are included in chapter 7.

2 Theoretical Background

If a beam of radiation, in any form of electromagnetic spectrum, penetrates a medium, the molecules and atoms of the medium can consume part of the incident energy and convert it into internal energy. Earth's top of atmosphere receives 1361 W/m^2 of solar electromagnetic radiation [15]. That electromagnetic radiation is transmitted through the atmosphere to Earth's surface, interacting with air molecules, aerosols particles, clouds, oceans, and landmasses. They absorb, scatter, and reflect part or all of the radiation, controlling how much radiation the Earth receives and how much it radiates back to the outer space. The radiative transfer is quantified by the radiative transfer equation (RTE) which allows to study and model the Earth's radiation [1]. The radiative transfer equation describes the change in radiation intensity I propagating through a medium via loss or gain due to extinction, scattering or emission

$$\frac{dI}{ds} = \underbrace{-(k_a + k_s)I}_{\text{extinction}} + \underbrace{\alpha B(T)}_{\text{thermal source}} + \underbrace{k_s \frac{1}{4\pi} \int_{4\pi} I(\omega')P(\omega, \omega')d\omega'}_{\text{scattering source}}, \tag{1}$$

where k_a and k_s are absorption and scattering coefficients respectively, $B(T)$ is the brightness temperature function, α is the absorptivity and $P(\omega, \omega')$ is the phase function giving the redirection of incoming intensity defined by ω' to the outgoing intensity defined by ω. The extinction term defines the loss of energy due to absorption and scattering while the thermal source term defines the gain of radiation due to emission, and the scattering source term when the scattering acts as a source, not a sink [1][4].

2.1 Absorption

Absorption of radiation by air molecules, clouds or aerosol particles is one of the two components of the extinction coefficient for the atmosphere. The intensity of incident radiation, the concentration of absorbing matter, and the effectivity of the absorber are the three factors that govern how much energy will be lost or absorbed. Assuming a thin layer of atmosphere with a infinitesimally small path length ds and incident radiation at wavelength λ with intensity I_λ (Figure 1), each air molecule (including trace gases) or aerosol particle interacts with the electromagnetic radiation decreasing the radiation by an increment:

$$dI_\lambda = -I_\lambda \sigma_a n ds, \tag{2}$$

where σ_a is the absorption cross-section and n the density of the medium. The density and absorption cross-section is defined by the absorption coefficient k_a

$$k_a(\lambda) = n\sigma_a \ . \tag{3}$$

Integrating Eq.[2] along the light path s leads to Beer-Lambert's law:

$$I(\lambda) = I_i e^{(-k_a \cdot s)}, \tag{4}$$

where I_i is the initial incident radiation beam and I is the transmitted beam.

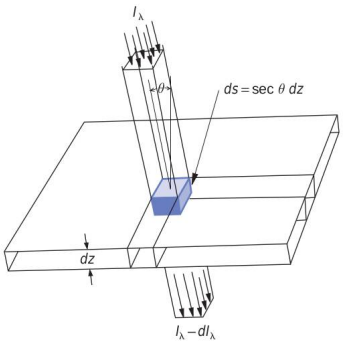

Figure 1: Absorption of incident solar radiation I_λ passing through an thin atmospheric layer ds containing absorbing gases and/or aerosols. (Wallace and Hobbs, 2005)

2.2 Scattering

Scattering is a physical process by which a particle in the path of an electromagnetic wave absorbs energy from the incident wave and re-radiates that energy in other direction[4]. Energy is removed from the light beam of photons by the interrupting particle which re-emits the energy again in different directions. The re-emission has the same inner energy if it is an elastic scattering event, or has a shift in energy equals to the rotational-vibrational energy of molecules in case of inelastic scattering event. As scattering is a function of wavelength and particle size, the size parameter x is important to define the scattering regime (Figure 2). For a spherical particle, x is defined as the ratio of the particle circumference to the incident wavelength λ [4]

$$x = \frac{2\pi r}{\lambda}, \tag{5}$$

where r is the scattering particle radius and λ is the wavelength of the incident beam.

If the particle size is much smaller than the wavelength of the incident beam then $x < 1$

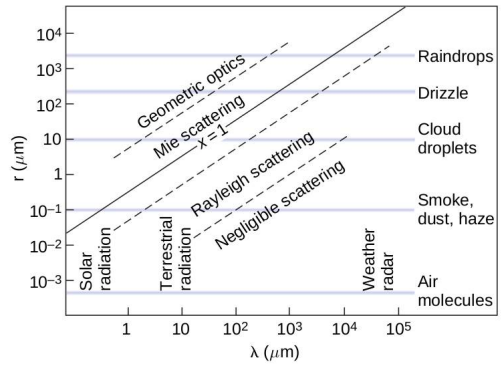

Figure 2: Scattering system plot based on size parameter (Wallace and Hobbs, 2005)[1]

and the light is scattered equally backward and forward (Figure 3.a). This is called Rayleigh scattering. When the particle size is almost equal to or larger than the wavelength then $x \gtrsim 1$, the light is scattered more in the forward direction (Figure 3.b). This may lead to much more complex patterns and features for example, in the case of a very big particle (Figure 3.c), where the forward scattering was scaled for representation purposes. This scattering at spherical particles is called Mie scattering.

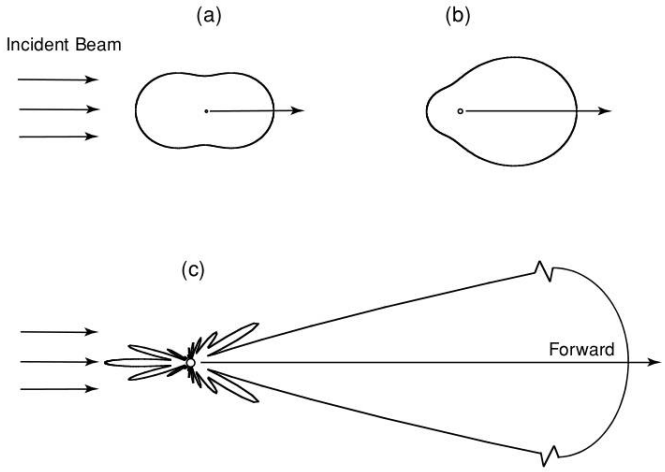

Figure 3: Scattering phase function of incident beam of wavelength $0.5\mu m$ by different aerosols particle sizes: (a)Rayleigh Scattering ($10^{-4}\mu m$), (b) 0.1 μm, and (c) Mie Scattering (1 μm) (Liou K. 2002)

The loss in intensity of radiation by scattering is treated the same as the absorption by introducing a scattering cross section σ_s

$$dI = -I_i \sigma_s(\lambda) n ds \tag{6}$$

and the scattering coefficient

$$k_s = n\sigma_s. \tag{7}$$

The sum of absorption and scattering coefficients defines the extinction coefficient k_e in the radiative transfer equation Eq. [1]

$$k_e = k_a + k_s. \tag{8}$$

Multiplying the amount of light coming from a given direction by the scattering probability, and integrating over all possible directions gives the intensity of radiation scattered

$$dI = k_s \frac{1}{4\pi} \int_{4\pi} I(\omega') P(\omega, \omega') d\omega' ds, \tag{9}$$

where $P(\omega, \omega')$ is the phase function that gives the scattered intensity distribution as a function of scattering angle (Figure 4).

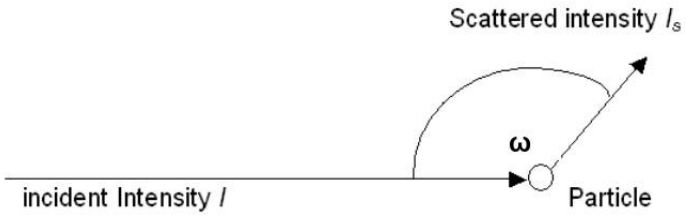

Figure 4: Phase function of scattering

2.2.1 Rayleigh Scattering

Rayleigh scattering is caused by small particles compared to the incident beam wavelength where charge displacement takes place and causes the molecules to move at the same frequency as the incident radiation. They start to radiate as dipoles with a change in the angular distribution of the scattered radiation[4]. The light is scattered equally forwards and backwards (Figure 3.a).
To explain Rayleigh scattering in terms of a dipole emitter, consider an unpolarized solar radiation beam of electric field E_0 is inducing a dipole moment p on an air molecule (scatterer), where α is the polarizability [5]

$$p = \alpha E_0. \tag{10}$$

The electric field can be represented by two equal and independent components inducing dipole moment components p_x and p_y. An induced dipole moment allows the accelerated charges to produce a scattered beam at angle Θ. Figure 5 shows the dipole emitters

schematically [5]. The solar beam of intensity I_0 is scattered by angle Θ and produces a scattered beam of intensity I which is given by [5]:

$$I(\omega, r) = I_0 k^4 \frac{\alpha^2}{r^2} \frac{(1 + cos^2\omega)}{2}, \tag{11}$$

while the phase function is given by:

$$P(\omega) = \frac{3}{4}(1 + cos^2\omega). \tag{12}$$

As the wavelength is $\lambda = 2\pi/k$, intensity and scattering coefficient are inversely proportional to the 4th power of wavelength [1]

$$k_\lambda \propto \lambda^{-4}. \tag{13}$$

The intensity can therefore be formulated in terms of wavelength and phase function as follows [5]:

$$I(\omega, r) = I_0 \frac{\alpha^2}{r^2} \frac{32\pi^4}{3\lambda^4} P(\omega). \tag{14}$$

The polarizability can be given in terms of scattering cross section for a single molecule as:

$$\alpha^2 = \sigma_s \frac{3\lambda^4}{128\pi^5}, \tag{15}$$

by substituting for Eq. [15] in the intensity formula Eq. [14], we derive that [5]:

$$I(\omega, r) = I_0 \frac{\sigma_s}{r^2} \frac{P(\omega)}{4\pi}. \tag{16}$$

2.2.2 Mie Scattering

Mie theory solves Maxwell's equations in terms of expansion in spherical harmonics and Bessel functions [4], where the particles' interactions with the radiation field are sufficiently separated and treated independently and the particle is assumed to be spherical. Scattered

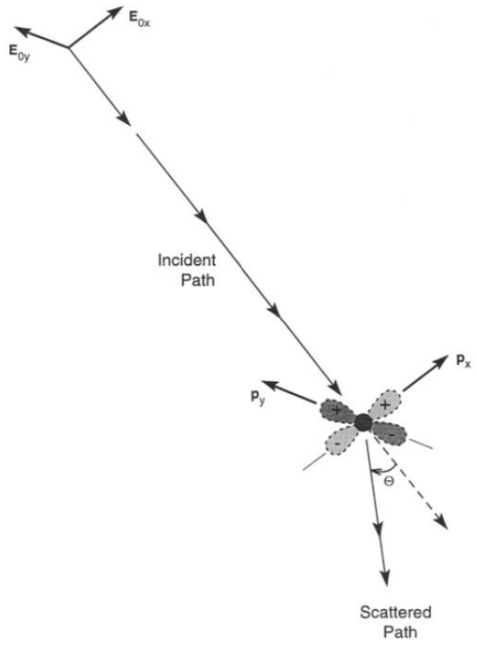

Figure 5: Rayleigh scattering in terms of dipole emitters. (Salby, 1996)

radiation includes: (a) the diffracted energy at the sphere and (b) the reflected energy inside the sphere [5]. The following expansion is used for scattering efficiency Q_s:

$$Q_s = \frac{\sigma_s}{\pi r} = c_1 x^4 (1 + c_2 x^2 + c_3 x^4 + ...), \tag{17}$$

where r is the radius. In the case of small particle $r \sim 10^{-4}\mu m$, the size parameter $x \sim 10^{-3}$ and the higher-order terms in the expansion can be neglected. The leading term is associated with Rayleigh scattering and is wavelength dependent. In the case of larger particles $r \gtrsim 10^{-1}\mu m$ Mie theory applies to describe radiation interaction with cloud droplets or aerosols and the size parameter is $x \gtrsim 1$. In this case, the scattering intensity is less wavelength dependent and primarily particle size-dependent [4].

2.3 Surface Reflectance

Light is reflected when it meets a boundary of a medium that does not absorb radiation strongly but it rebound the waves, and the boundary separates two media of different densities [6]. In addition to absorption and scattering, a fraction of sunlight is reflected by earth's surface, the fraction and the direction of reflected light depends on the surface and its elements. Figure 6 shows the direction of incident and reflected radiative flux, where θ_0 is the solar zenith angle, θ is the angle between the zenith and the observer known as the

view zenith angle, Φ is the relative azimuth angle, and Θ is the scattering angle.
In many cases considered in numerical radiative transfer, the spectral albedo is the ratio between the upward reflected radiative flux F_λ^+ and the incident downward radiative flux F_λ^-. The radiative flux is the the power per unit area per unit wavelength interval which is also referred to as irradiance[7]

$$\alpha_\lambda = \frac{F_\lambda^+}{F_\lambda^-}. \tag{18}$$

The albedo is defined as the ratio between upward reflected irradiance and the downward incident irradiance. Albedo is difficult to be measured directly, so the surface is assumed to reflect isotropically (Lambertian surface). Due to its importance in remote sensing and climate studies, it was necessary to find an approach to estimate the albedo or spectral hemispherical reflectance of real surfaces that often reflect anisotropically [8]. The Bidirectional Reflectance Distribution Function (BRDF) is introduced to improve the surface treatment using a simple Lambertian assumption and describe the surface reflectance as a function of two directions, the incident and outgoing. Each direction is described by two angles: zenith and azimuth, which are defined with respect to the surface normal (Figure 6). The function returns the ratio of reflected radiance and irradiance incident on the surface.
The BRDF is an approximation of the Bidirectional scattering-surface reflectance distribution function or Bidirectional surface scattering (BSSRDF) as it ignores sub-surface scattering [9]. The model used to describe BRDF in this work is explained in section 3.5. The function is formulated as in Gatebe and King [10], where dL is the observed irradiance and dE is the incident radiation:

$$f(\theta_s, \theta_v, \phi, \lambda) = \frac{dL(\theta_s, \theta_v, \phi, \lambda)}{dE(\theta_s, \phi, \lambda)}. \tag{19}$$

2.4 Aerosol Optical Thickness (AOT)

A fraction of incident solar radiation is lost when it passes through the atmosphere due to absorption and/or scattering by aerosols and clouds. The depletion of radiation by aerosols is an important parameter for atmospheric studies and called Aerosol Optical Depth (AOD) or Aerosol optical Thickness (AOT). Both terms are often used synonymously, the second term will be used in this manuscript. AOT is the vertical integral of the extinction coefficient (sum of absorption and scattering coefficients) over the vertical atmospheric column to the zenith angle [1]. By integrating the extinction coefficient from the top of atmosphere to level

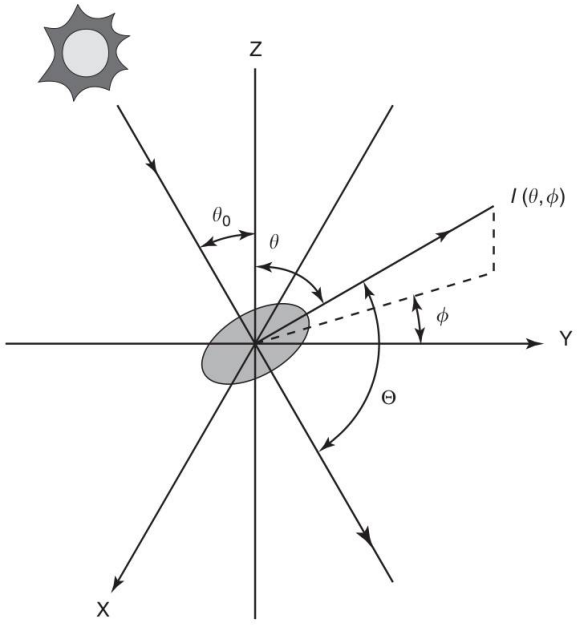

Figure 6: Geometry of solar reflectance [7].

z the AOT formula is given as follows:

$$\tau(\lambda) = \int_z^\infty k_e dz, \tag{20}$$

where τ is the optical thickness, and k_e is the aerosol extinction coefficient.
AOT is a metric of aerosol concentration and its impact on the atmospheric radiative transfer. It cannot be measured directly, so it is retrieved by computer models to simulate the atmospheric radiative transfer. SCIATRAN is the model used in this work to retrieve AOT and is discussed in more detail in section 3.4.

3 Data and Instruments

In this study, the POLDER third-generation radiometer data onboard PARASOL (Polarization Anisotropy of Reflectances for Atmospheric Sciences coupled with Observations from a Lidar) mission is the main input dataset to the SCIATRAN radiative transfer model to retrieve AOT. The data from the ground network AERONET (AErosol RObotic NETwork) is used to validate the retrieval process output. In order to investigate the validation and retrieval performance, some auxiliary datasets from the Aqua/MODIS mission are used. Auxiliary datasets are cloud fraction, RGB images, and land cover.

3.1 POLDER/PARASOL

3.1.1 Instrument

The Polarization and Directionality of the Earth's Reflectances (POLDER) instrument is a space-borne optical imaging radiometer and polarimeter developed by the French CNES (Centre national d'études spatiales). The first generation of the instrument was selected to fly aboard the Japanese ADEOS I satellite launched in August 1996. ADEOS I ended about one year later and was followed by ADEOS II in December 2002. ADEOS II carried the second generation of the instrument POLDER-2. Due to the short lifetime of ADEOS II mission, the POLDER instrument which is similar to that of POLDER-1 and POLDER-2 on ADEOS II was launched again in December 2004, this time on the space segment PARASOL. It was designed for climate change and global environmental studies observing the polarized, unpolarized, and directional solar radiation reflected by the atmosphere. The POLDER radiometer consists of three components: a CCD sensor of 242x274 independent sensitive pixels, a rotating wheel with a steady period of 4.9s carrying polarizers to select the polarization directions, and spectral filters to select the spectral bands, and wide field of view (FOV) telecentric optics [11].
The instrument provides data in 9 different spectral bands, as shown in (Table 1) [12]. They are defined by their central wavelength, bandwidth, and polarization. The rotating wheel carries 16 slots, 9 of them are polarized filters (3 polarization directions for 3 different wavelengths) and 6 are unpolarized filters. There is one opaque slot for dark current estimation [12].

The POLDER instrument is imaging on the sunlit side of the satellite orbit only. The acquisition sequence is repeated every 19.6 seconds. A sequence is composed of 16 image acquisitions in the following order: Dark, 490P1, 490P2, 490P3, 443, 1020, 565, 670P1,

POLDER Band	443P	490NP	565NP	670P	763NP	765NP	865P	910NP	1020NP
Central Wavelength (nm)	443.9	491.5	563.9	669.9	762.8	762.5	863.4	906.9	1019.4
Band Width (nm)	13.5	16.5	15.5	15.0	11.0	38.0	33.5	21.0	17.0

Table 1: POLDER spectral bands, (P):Polarized, (NP): Not Polarized [12].

670P2, 670P3, 763NP, 765NP, 910NP, 865P1, 865P2, 865P3. Each produces measurements of a spatial resolution of 6x7 km^2 per pixel.

3.1.2 Data Processing

The POLDER data are processed by CNES in Paris from level-0 to level-3. The data used in this work is level-1 data, given as sun-normalized radiance. The data were calibrated, geometrical corrections and cloud masking were applied. Radiometric processing was completed including stray light correction, subtraction of "dark current", and computation of Stokes parameters (I, Q, U) from the three measurements for each of the three polarized bands [12]. In this study, V1.01 level-1 data has been used, which were downloaded from: `ftp://ftp.icare.univ-lille1.fr/SPACEBORNE/PARASOL/L1_B-HDF.v1.01/`.
The AOT retrieval is very sensitive to clouds and land cover. The POLDER/PARASOL dataset has been processed using a cloud detection and rejection scheme utilizing multi-spectral and multi-directional capabilities of the instrument. The scheme consists of fours tests applied for each acquired pixel.
Clouds gives the large reflectance values in the blue band (440 nm), while most land covers are associated with low reflectance values in this band and vary more in the VIS-NIR bands. The first test is called "Blue Channel threshold" and is taking advantage of this fact. The test applies a threshold to exclude cloudy pixels with high response in the blue band channel $R(440nm) > R_{threshold}$. This test is not sufficient for thin clouds and smoke plumes. It only produces good results with vegetation land cover but is limited over desert, urban, and snow land covers.
The second test is the "Apparent pressure filter", which requires two channels of POLDER centered over the oxygen « A » absorption band at 765 nm with different widths. One is narrow with a width of 10 nm and one is wider having 40 nm width. The formula for apparent pressure is derived as a function of the ratio between two channels and the viewing geometry. The apparent pressure P_{app} is compared to surface pressure P_{surf}. This comparison allows detecting cloud presence since these scattering layers (in particular high clouds) have a large effect on the apparent pressure, where $P_{surf} - P_{app}(760nm) > \Delta P$. The NDVI (Normalized difference vegetation index) is a vegetation index used to measure the status of plants, it is formulated as a ration between the difference in the intensities of reflected light in the red

and infrared range to the sum of these intensities. The second test is NDVI-dependent due to the high spectral variation of vegetation reflectance around 700 nm wavelength and not sufficient for low altitude clouds.
The third test exploits the polarization properties of clouds. The water droplets exhibit maximum scattering at 142 deg from the incoming direction. The maximum is highly polarized, so it is detected using polarization measurements. This polarization rainbow test uses an 860 nm channel, where atmospheric molecules' single scattering effects are small. The test is limited to the availability of the needed scattering angle. The 142-degrees angle is acquired only for about 60% of observed pixels.
The fourth test checks pixels adjacent to a detected cloud and flags them contaminated. These pixels are rejected for further processing. In summary, POLDER/PARASOL is introducing an effective cloud masking scheme for thick clouds and high clouds over vegetation, and forests land covers. But it is not sufficient for thin clouds, smoke plumes, and low clouds. It is also limited when it is used for desert, urban, and snow covers. The scheme is explained in detail in Bréon and Colzy (1999)[16]

3.2 AERONET

3.2.1 Instrument

The AERONET (AErosol RObotic NETwork) is a network of more than 1500 ground-based remote sensing stations, provided by a multi-band sun photometer of the most recent model of Cimel [13]. It can perform measurements for both spectral sun irradiance and sky radiances and spectral lunar irradiance at several fixed wavelengths within the visible-near-infrared spectrum [14]. It provides long-term and globally distributed observations of spectral AOT and inversion products such as aerosol volume size distribution, aerosol complex refractive index, optical absorption, and the aerosol scattering phase function [14]. The radiometers make two basic measurements, direct sun or sky radiance measurements. The direct sun measurements are made in 8 spectral bands 340, 380, 440, 500, 670, 870, 940, and 1020 nm. At each wavelength, the optical depth is calculated from the spectral extinction of the radiation beam. The aerosol optical thickness is isolated by estimating and removing the contribution by Rayleigh scattering, Ozone absorption, and other absorbents in the spectrum [13]. The sky radiance measurements are made in 4 spectral bands 440, 670, 870, and 1020 nm. The measurements are inverted using Dubovik [36] and Nakajima [37] inversion algorithms. The latter inversion algorithm retrieves aerosol properties, size distribution, and phase function over the particle size range of 0.1 to 5 μm.

3.2.2 Data Description

AERONET collected data are processed for three quality levels, Level 1.0 (unscreened), Level 1.5 (cloud-screened). The processing includes several algorithms : (1) AOT retrieval, (2) AOT cloud screening, (3) SeaPRISM [2] processing, and (4) sky radiance data (Almucantars and Principal Planes) inversion. Once these data were manually inspected, they were manually upgraded to level 2.0 (quality-assured and cloud screened) [13].

AERONET data are distributed via the internet through a web tool and FTP network protocol. Data version 3.0 at level 2.0 are used in this study and have been downloaded from `https://aeronet.gsfc.nasa.gov/data_push/V3/AOD/AOD_Level20_All_Points_V3.tar.gz` (downloaded on 30.06.2021). The AERONET measurements have an uncertainty of approximately 0.01 - 0.02 in AOT (wavelength dependent) due to calibration uncertainty for the field instruments [13].

A temporal variability method is used for AERONET cloud screening. Data are acquired in triplet sequence measurements of 30-second intervals. The optical depth of clouds is temporally varying faster than the one of aerosols. Thus, a threshold accounting for this variability is used to discriminate clouds and aerosols. Under stable conditions, the threshold is set to ≈ 0.02 while it is ≈ 0.03 during biomass or heavily loaded aerosol conditions. As the algorithm depends also on temporal variation of τ, variable aerosol plumes could be erroneously also be screened as clouds. A stable uniform cloud will pass the algorithm [17].

3.3 Aqua/MODIS

One[3] MODIS (Moderate Resolution Imaging Spectroradiometer) instrument is flying aboard Aqua (originally known as EOS PM-1) satellite. Aqua travels from south to north, crossing the equator in the afternoon. For that reason, it was selected in this study as it is part of the afternoon constellation known as A-Train. The constellation included, for the period of 2004 to 2009, POLDER/PARASOL with 3 minutes passing time difference relative to Aqua/MODIS as shown in (Figure 7).

Aqua/MODIS is scanning Earth's surface with a scan rate of 40.6 scans per minute. That enables it to view the whole planet's surface every 1 to 2 days in 36 spectral bands with high

[2] SeaPRISM is a CIMEL CE-318 automated sun photometer modified to perform above-water radiometric measurements in addition to the regular atmospheric measurements defined for NASA's Aerosol Robotic Network (AERONET)

[3] Another MODIS instrument not considered here is flying on Terra, because the instrument has an another orbit

radiometric resolution. The bands range in wavelength from 0.4 µm to 14.4 µm. The two-mirror off-axis optical system directs energy to four refractive objective assemblies; one for each of the VIS, NIR, SWIR/MWIR, and LWIR spectral regions to cover the mentioned spectral range. Two bands are imaged at a nominal resolution of 250 m at nadir, with five bands at 500 m, and the remaining 29 bands at 1 km. The Aqua orbit of 705 km achieves a width of 2330 km.

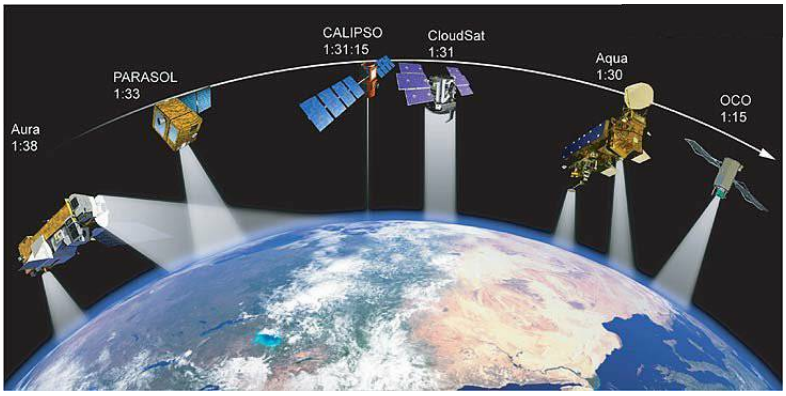

Figure 7: The Afternoon constellation. (https://atrain.nasa.gov/)

MODIS Level 1 data products are available 1) Level-1A product geolocation at 1000 meter resolution. It is called MYD03 product for Aqua. 2) Level-1B is radiance at 1000, 500, and 250-meter resolution and is called MYD021KM, MYD02HKM, MYD02QKM respectively for Aqua. Both products are necessary for producing true color images.

3.3.1 True color images

Natural-looking images in RGB format are produced using the MODIS Corrected Reflectance algorithm (Figure 8). The algorithm, developed by Jacques Descloitres at NASA/GSFC, utilizes MODIS Level 1A-B data (the calibrated, geolocated radiances). Although it is not a standard product, it supports the visual identification of clouds and smoke plumes in this study. The algorithm is removing the undesired atmospheric effects from the visible bands 1-7. The data is provided in near real-time. The sensor resolution is 500 m and 250 m (bands 1 and 2 have a sensor resolution of 250 m, bands 3 – 7 have a sensor resolution of 500m, and bands 8 - 36 are 1 km. band 1 is used to sharpen Band 3, 4, 6, and 7), imagery resolution is 250 m, and the temporal resolution is daily. The product could be hazy sometimes due to algorithm limitations but still sufficient for visual inspection [18].

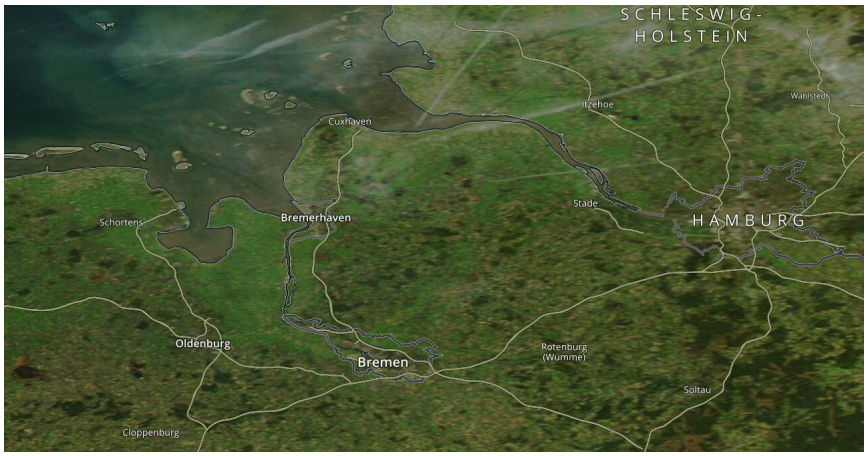

Figure 8: True color image from Aqua/MODIS

3.3.2 Cloud Fraction Product

The MODIS Cloud Fraction is a measure of the percentage of Earth's surface covered by clouds (Figure 9). The product provides the possibility to evaluate the POLDER/PARASOL cloud masking qualitatively. The evaluation method is explained in Chapter 5. The MODIS Cloud Fraction layer indicates the fraction of pixels within a 25 square kilometer box (5x5 1 km pixels) that are determined to be confident or probably cloudy by the MOD/MYD35 1km x 1km Cloud Mask. The MODIS Cloud Fraction layer is available for Aqua (MYD06) satellite day and night. The sensor/algorithm resolution is 5 km, imagery resolution is 2 km, and the temporal resolution is daily [19].

Figure 9: Cloud fraction product from Aqua/MODIS

3.3.3 Land cover type product

MODIS Land Cover Type product provides information about the land cover type in the vicinity of AERONET stations (Figure 10). The product is derived using supervised classifications of MODIS Terra and Aqua reflectance data [20]. Prior knowledge and supplemental information are fed into the algorithm to refine the categorized classes. The land cover type is defined according to the International Geosphere-Biosphere Programme (IGBP) classification scheme (Table 2) [20].

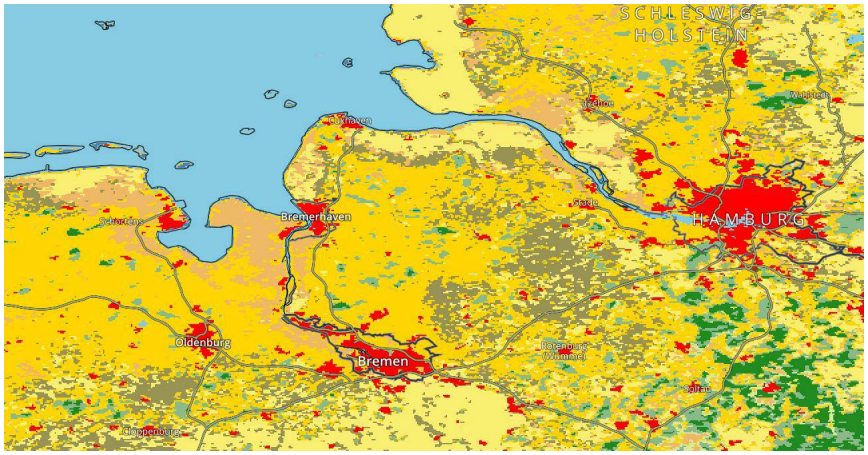

Figure 10: Land cover type product from Aqua/MODIS

Figure 11: Land cover type legend

IGBP legend and class descriptions	
Name	Description
Evergreen Needleleaf Forests	Dominated by evergreen conifer trees (canopy > 2m). Tree cover > 60%.
Evergreen Broadleaf Forests	Dominated by evergreen broadleaf and palmate trees (canopy >2m). Tree cover > 60%
Deciduous Needleleaf Forests	Dominated by deciduous needleleaf (larch) trees (canopy > 2m). Tree cover > 60%.
Deciduous Broadleaf Forests	Dominated by deciduous broadleaf trees (canopy > 2m). Tree cover > 60%.
Mixed Forests	Dominated by neither deciduous nor evergreen (40-60% of each) tree type (canopy >2m). Tree cover >60%.
Closed Shrublands	Dominated by woody perennials (1-2m height) > 60% cover.
Open Shrublands	Dominated by woody perennials (1-2m height) 10-60% cover.
Woody Savannas	Tree cover 30-60% (canopy > 2m).
Savannas	Tree cover 10-30% (canopy > 2m).
Grasslands	Dominated by herbaceous annuals (< 2m).
Permanent Wetlands	Permanently inundated lands with 30-60% water cover and > 10% vegetated cover
Croplands	At least 60% of area is cultivated cropland.
Urban and Built-up Lands	At least 30% impervious surface area including building materials, asphalt, and vehicles
Cropland/Natural Vegetation Mosaics	Mosaics of small-scale cultivation 40-60% with natural tree, shrub, or herbaceous vegetation
Permanent Snow and Ice	At least 60% of area is covered by snow and ice for at least 10 months of the year.
Barren	At least 60% of area is non-vegetated barren (sand, rock, soil) areas with less than 10% vegetation.
Water Bodies	At least 60% of area is covered by permanent water bodies
Unclassified	Has not received a map label because of missing inputs.

Table 2: International Geosphere-Biosphere Programme (IGBP) legend and class descriptions [20].

4 SCIATRAN Radiative Transfer Software

4.1 Model Overview

The physical processes mentioned in chapter 2, such as absorption, scattering, reflection, and polarization, have been effectively used to describe the atmospheric radiative transfer processes happening within the Earth's atmosphere. In this study, we have used SCIATRAN [21], a radiative transfer modeling software package to precisely retrieve Aerosol optical thickness (AOT). SCIATRAN is developed to solve numerous forward and inverse problems for the terrestrial atmosphere and ocean. It contains solvers with a finite difference and discrete-ordinate techniques and an extensive database. For spectral range from the ultraviolet to the thermal infrared (0.18-40μm), SCIATRAN is considering different radiative transfer processes such as absorption by gaseous components, Rayleigh scattering, scattering by aerosol and cloud particles, and bidirectional reflection from the underlying surface including Fresnel reflection from a flat as well as rough ocean surface. It is also able to simulate the radiative transfer in the scalar or the vector mode [21]. SCIATRAN takes the data from various platforms as input, such as balloon-borne (space, air, or ship), ground-based, and underwater instruments. The measurements could be given in various geometry orientations e.g. nadir, off-nadir, limb, zenith-sky, or occultation. Assuming plane-parallel or a spherical atmosphere, SCIATRAN is capable of modeling spectral and angular distributions of the intensity or the Stokes vector of transmitted, scattered, reflected, and emitted radiation. It is downloaded from the following link: `https://www.iup.uni-bremen.de/sciatran/`

4.1.1 Model Features

SCIATRAN radiative transfer model has many features, the main features are described as follows: 1) *Spectral range and information*: as mentioned previously SCIATRAN is designed to operate in the spectral range from the ultraviolet to the thermal infrared (0.18-40μm). This is the range where radiative transfer calculations are usually performed. The O_2 Schumann–Runge bands and Herzberg continuum are implemented for calculations of photolysis frequencies. The SCIATRAN database includes spectral information for absorption cross-sections at resolution from 0.24 to 0.54 nm based on the used spectral range. 2) *Model geometry*: to obtain a wider range of illumination and observation conditions, SCIATRAN can operate under several geometry assumptions such as plane-parallel, pseudo-spherical, approximative spherical, and fully spherical modes. But the fully spherical solution is implemented only for the scalar mode. 3) *Atmosphere*: SCIATRAN

is provided with databases of optical characteristics of water (spherical droplets) and ice (fractal particles, hexagonal crystals) clouds. In addition it contains several databases of aerosol optical characteristics including the widely used LOWTRAN 7 parameterization [26]. The provided databases allow modeling absorption by atmospheric trace gases, Rayleigh scattering, aerosols, and clouds. 4) *Surface reflection*: the Bidirectional reflectance distribution function (BRDF) is used for modeling the land surface reflectance. It is implemented according to the RPV (Rahman-Pinty-Verstraete) model or Ross-Li model, the latter is considered in this study and discussed in chapter 4.2. SCIATRAN is one of the few freely available software capable of modeling radiative transfer through a coupled ocean-atmosphere system. SCIATRAN can be run assuming either a flat or wind-roughed air-water interface [21].

4.1.2 Atmosphere optical characteristics in SCIATRAN

The radiative transfer in the atmosphere is governed by several processes like molecular scattering, absorption, and scattering by aerosol and cloud particles, the absorption by gaseous species, and thermal emission. The extinction and scattering coefficients, phase functions, or scattering matrices (scalar or vector case, respectively) are the related optical characteristics of the atmosphere and reflecting properties of the underlying surface. They are necessary for the numerical solution of an uncoupled atmospheric problem. SCIATRAN uses a database to calculate these parameters. The databases contain information on molecular scattering characteristics, optical characteristics of aerosols and clouds, vertical distributions, and spectral characteristics of gaseous absorbers, in addition to vertical profiles of the pressure and temperature. The database of atmospheric parameters in SCIATRAN, for the used version (v4.0.13) in this study, is described as follows:

A. Rayleigh scattering: described in chapter 2.2.1 is characterized by the scattering coefficient and scattering matrix. The first is defined as the fraction of light scattered by air molecules per unit distance, while the latter is used to define the direction of scattered light based on the angular distribution in terms of the depolarization factor [24]. The Earth's atmosphere is mainly composed of N_2 and O_2. As both of them are diatomic, the air has a slightly anisotropic polarizability. This slight anisotropy of the air is explained by the depolarization factor. The depolarization factor is weakly dependant on the wavelength at the range from 300 to 800 nm. The SCIATRAN software provides either a constant or wavelength-dependent depolarization factor [21]. The Rayleigh scattering coefficient is a function of the Rayleigh scattering cross-section and the molecular number density. At

wavelength λ, the cross-section is given by Eq.[15]. But Eq.[15] is not directly used in this context, because the depolarization term and refractive index of the air need to be taken into account. As both of them do not have an exact analytical representation, approximations are needed. SCIATRAN implements the most commonly used approximation such as modified Bates approximation [38], Bucholtz approximation [39], and Bodhaine approximation [40]. In addition to a User-defined mode that allows experienced users to select and use other combinations of approximations. See Rozanov et al. (2014) [21] for more details.

B. Atmospheric aerosol: SCIATRAN uses the aerosol layer concept, where the atmospheric column is divided into several layers. Each is defined by the altitude for the upper and lower boundary of the layer. Aerosol optical characteristics are assumed to be invariant in the same layer, but the aerosol number density is changing. The optical characteristics used to describe light scattering by aerosols are extinction and scattering coefficients in addition to the scattering matrix. Both extinction and scattering coefficients are expressed as the products of the aerosol number density and the corresponding cross-sections.

The SCIATRAN model, in default mode, assumes aerosol particles of a spherical shape, while non-spherical or in-homogeneous particles cannot be accounted for. Particle size distribution and a refractive index for each aerosol type need to be specified. The aerosol characteristics can be introduced in two ways. In the user-defined mode, they can be specified by the user. By providing profiles of the aerosol extinction and scattering coefficients as well as the scattering matrix for each aerosol layer at a desired number of wavelengths. On the other hand, they can be read from the internal databases (WMO, SCIATRAN, and LOWTRAN 7). Based on the World Meteorological Organization (WMO) recommendations, the so-called WMO database provides applicable aerosol parameterization for the entire spectral range used in SCIATRAN in both scalar and vector mode calculations. The recommendations include information about the particle size distributions and spectral refractive indices for six basic components of the atmospheric aerosol: the water-soluble, dust, oceanic, soot, stratospheric, and volcanic aerosols. For the scalar (unpolarized) radiative transfer calculations, SCIATRAN and LOWTRAN 7 [26] databases are incorporated in the software package. The internal aerosol database of SCIATRAN is calculated by Mishchenko et al. (1999)[25] code, which is publicly available at `http://www.giss.nasa.gov/staff/mmishchenko/brf/`. It provides information about the various basic components of the aerosol, based on the database compiled by Koepke and Hess [27], while the user can provide the aerosol number density or calculate it from the aerosol extinction coefficient profile. The SCIATRAN database covers the spectral range from 225 nm to 2.5 μm. While the LOWTRAN 7 database covers the spectral range from 200 nm to 6 μm.

The LOWTRAN 7 is the third database used in the SCIATRAN software package. It contains information about several pre-defined aerosol compositions that cannot be changed independently. The LOWTRAN 7 describes two sections of the atmosphere. The lower atmosphere is where the user can adjust the aerosol properties according to the humidity and visibility parameters. The stratosphere where aerosol parameterizations correspond to background atmosphere. The scattering/extinction coefficient and phase function are also included.

In this study, the so called MODIS dark target product (Levy et al., 2007) [41] is utilized by SCIATRAN to prescribe aerosol types. We can deduce the complex refractive index and the particle size distribution along with the retrieval of the AOT at 0.55 µm based on Levy et al. (2007) assumption that the intrinsic properties of the aerosol are related to the loading. They were able to describe a framework connecting the aerosol micro-physical properties (refractive index and size distribution) to AOT at 0.55 µm.

C. Clouds: Water droplets and ice crystals are the components of Earth's atmosphere clouds. Both components scatter light similar to how aerosols do. Luckily, their refractive indices are known what makes it easier to parameterize clouds more than aerosols. SCIATRAN defines clouds as layers with user-specified lower and upper boundaries. While the optical characteristics for each cloud layer are specified by the user or read from internal databases in SCIATRAN. The model has two databases: one for water clouds and the other for ice clouds, both could be combined also to parameterize mixed clouds [21].
The optical characteristics of water droplets are, the scattering and extinction cross-sections as well as scattering matrices, calculated using Mie theory mentioned in chapter 2.2.2. In SCIATRAN, these calculations are done at 451 spectral steps between 0.2 and 40 μm and incorporated in the water clouds database. On the other hand, ice crystals' optical characteristics are described using geometrical optics approximations. The SCIATRAN ice cloud database calculates these approximations using the ray-tracing Monte-Carlo code, it assumes randomly oriented cloud particles represented as fractal particles or hexagonal prisms. The calculations are done at 73 different wavelengths within the range of 0.2 to 40 μm. Significant errors can arise due to the limited validity of the geometrical optics approximation. In addition to combining water and ice databases, SCIATRAN provides the option to introduce a vertical inhomogenties of cloud optical characteristic [21].

D. Gaseous absorbers, pressure, and temperature : Atmospheric trace gases with significant absorption signatures are crucial for radiative transfer modeling. Consequently, their concentration, dependency on temperature and pressure are needed. A climatological database is incorporated in SCIATRAN. It includes the zonally and monthly averaged distribution of atmospheric trace gases, pressure, and temperature information. The database

could be obtained from a 2D chemical transport model developed at the University of Bremen [28], a 2D chemical transport model developed at MPI Mainz [29], or a globally averaged US standard model atmosphere [30]. SCIATRAN is offering flexibility, as the users can switch easily between using their own climatological information or reading them from database contents based on their needs [21].
The common absorbers included in the database are (O_3, NO_2, SO_2, ClO, $HCHO$, BrO, NO_3, $OClO$, O_2, H_2O, CO_2, N_2O, CO, CH_4, NO, NH_3, HNO_3, OH, HF, HCl, HBr, HI). Their absorption features can be accounted for based on the spectral range and required accuracy. In UV-Vis spectral range, Ozone absorption bands such as Hartley, Huggins, and Chappuis (Figure 12) have very significant spectral impact. The absorption cross-sections have an intermediate dependency on temperature and less dependency on pressure. So, the cross-sections are measured at different temperatures or using parameterization. The NIR-TIR spectral range shows a strong dependency on pressure and temperature. To account for these spectral signatures accurately, a line-by-line calculations approach is used at very high spectral sampling. The information of each wavelength (e.g. line positions and intensities) are provided by the HITRAN (HIghresolution TRANsmission) database [31]. In the SCIATRAN model, absorption features of the following molecules can be calculated using the HITRAN database: O_3, NO_2, SO_2, ClO, $HCHO$, O_2, H_2O, CO_2, N_2O, CO, CH_4, NO, NH_3, HNO_3, OH, HF, HCl, HBr, HI [21].

4.1.3 Standard Outputs

This section describes the standard outputs that can be obtained using the SCIATRAN radiative transfer model. The outputs include several radiometric quantities such as the radiance, the upward, downward, and diffuse fluxes, actinic flux, and the downward direct flux [21]. The radiance is the power of an electromagnetic wave per unit area per unit spectral interval per unit solid angle. SCIATRAN can model the radiance at different viewing angles, solar zenith angles, observer altitudes, and wavelengths. The actinic flux is the spherically integrated flux including solar direct beam and scattered components [32]. It is responsible for initiating the chemical processes in the atmosphere. It is however irrelevant to the goals of this study.
This study is concerned more with the vertical optical thickness (VOT) output. SCIATRAN provides VOT as a function of the wavelength λ for the extinction of both clouds and aerosols Eq.[20]. This output is used also to calculate the vertical optical thickness of main gaseous absorbers mentioned in chapter 4.1.2 in different spectral ranges [21]. The SCIATRAN model calculates the Stokes parameters and ellipsometric parameters in vector mode, to consider the polarization process. The Stokes parameters are expressed in the units (sr^{-1}).

The ellipsometric parameters include the degree of polarization, degree of linear and circular polarization, ellipticity, and polarization angle.

As this study is considering a retrieval algorithm of AOT, it takes the advantage of using the so-called weighting functions provided by SCIATRAN see chapter 4.3. The following parameters are calculated using the weighting functions features in SCIATRAN [21]: number density of all atmospheric gaseous absorbers included in SCIATRAN; scattering and absorption coefficients of aerosols; aerosol optical thickness; BRDF; scattering and absorption coefficients of clouds; cloud properties: effective radius of particles, particle number density, liquid and ice water content; cloud extension: top and bottom heights, optical thickness; pressure and temperature; surface elevation and Lambertian surface albedo

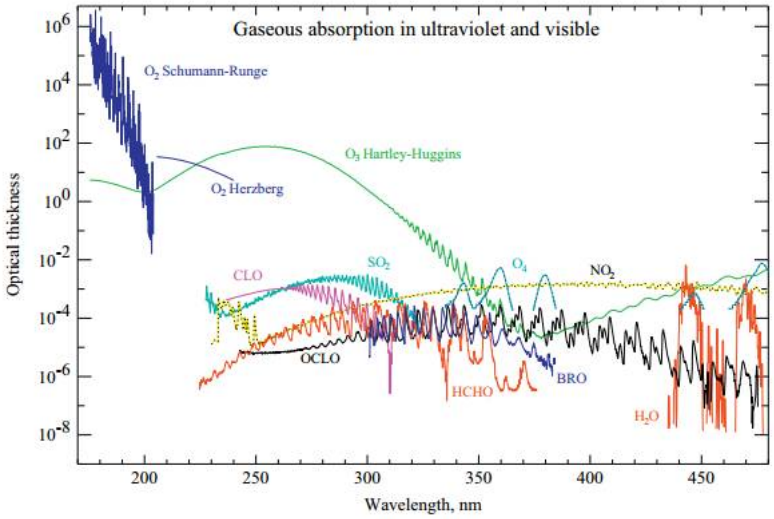

Figure 12: Vertical optical thicknesses of main gaseous absorbers in UV–Vis spectral ranges, showing Ozone absorption bands Hartley, Huggins, and Chappuis in green. (Rozanov et al, 2013)

4.2 BRDF

Anisotropic reflectance of the Earth's surface is a critical component of the remotely sensed received signal from space. Bidirectional Reflectance Distribution Function (BRDF) describes the surface reflectance as a function of two directions, the incident and outgoing. Each direction is described by two angles: zenith and azimuth, which are defined with respect to the surface normal (Figure 6). The function returns the ratio of reflected radiance and irradiance incident on the surface. Several BRDF models were developed to reproduce the strong angular variability related to surface bidirectional effects such as Ross-Li model and the nonlinear Rahman–Pinty–Verstraete (RPV) model.

As mentioned previously, multi-viewing POLDER measurements are used in this study to retrieve the aerosol optical thickness. It was important to carefully select the best model to describe the surface reflectance. Maignana et al., (2004) [33] evaluated the ability of several analytical models to reproduce the observed directional signatures. The study concluded that the three-parameter linear Ross–Li model and the nonlinear Rahman–Pinty–Verstraete (RPV) model are the best. As a part of the previous work by Vountas et al. (2020) [2], the two BRDF models, the Ross-Li and the modified Rahman-Pinty-Verstraete-facet (mRPV-facet) were compared over vegetation dominated surfaces. The comparison revealed that Ross-Li model is more effective to describe the surface reflectance over the study region of Vountas et al. (2020) using SCIATRAN [2].

Thus, the kernel-based Ross-Li model is used in this study. It considers the observed surface reflectance as the sum of three components [23]: (1) the diffuse reflection due to *geometrical* structure opaque reflectors, including shadowing effect, (2) *volume* scattering properties of canopies and bare soil, and (3) the *isotropic* reflectance. The semi-empirical BRDF model can be given by simple linear form [22]:

$$BRDF = f_{iso}(\lambda) + f_{vol}(\lambda) \cdot K_{vol}(\theta_i, \theta_v, \phi) + f_{geo}(\lambda) \cdot K_{geo}(\theta_i, \theta_v, \phi), \qquad (21)$$

where f_{iso} is a constant representing the isotropic reflectance of the surface, K_{vol} and K_{geo} are the volumetric kernel to describe the second component in Eq. [21] and the geometric kernel to describe the last component, respectively. Both kernels are functions of the viewing zenith angle θ_v, illumination zenith angle θ_i and relative azimuth angle ϕ, and f_{vol} and f_{geo} are the weights for the volumetric and geometric kernels, respectively.

Belinska (2019) [34] used the Ross-Li BRDF model in SCIATRAN and compared it to POLDER data of the same version and data level used in this study. The comparison showed

good agreement between SCIATRAN simulated sun normalized radiance and POLDER observations (Figure 13). Consequently, the same setting as Belinska (2019) is considered for the Ross-Li model implementation in SCIATRAN. The settings adapt parameters for grassland and cropland from Knobelspiesse et al. (2008) [35].

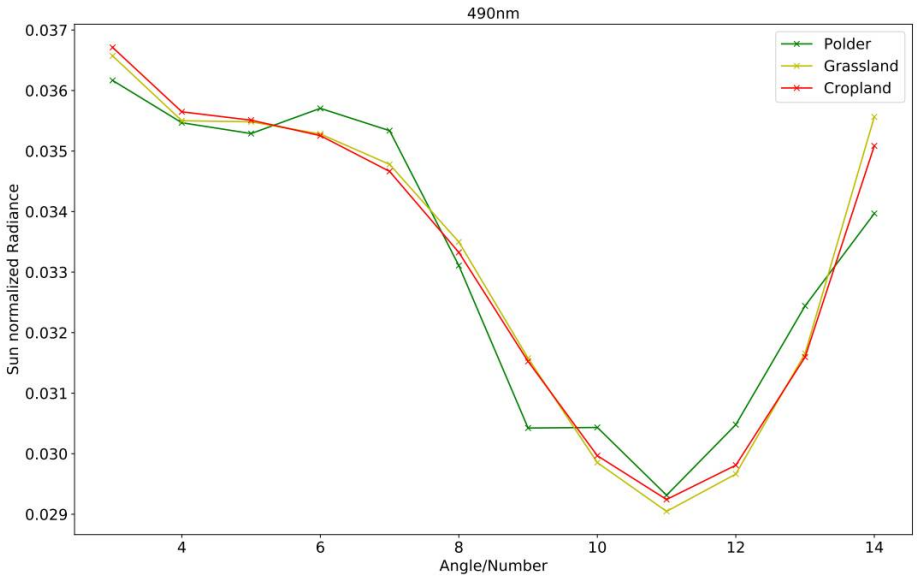

Figure 13: Sun normalized radiance as a function of the angle number from a SCIATRAN simulation with parameters from Knobelspiesse et al. (2008) for grassland and cropland and POLDER data from the 490 nm channel. (Belinska, 2019)

4.3 AOT Retrieval process

The following underlying considerations are relevant for the retrieval: a) POLDER channels have been selected where gas absorption can be neglected, b) only cloud-free conditions are considered, c) and so far it is neglecting polarization [2]. Therefore, the governing factors of a signal, either modeled or measured are aerosol loading, atmospheric molecular scattering, and surface reflectance. Assuming that atmospheric molecular scattering (Rayleigh Scattering) is modeled accurately, and from Eq.[21], the variation of spectral reflectance is presumed to be defined with respect to Ross-Li model coefficients k_i and the variation of aerosol particle number density $N(z)$ as:

$$\Delta R(\lambda, \Omega) = \int_0^H W_N(z, \lambda, \Omega)\delta N(z)dz + \sum_{i=1}^{3} W_i(\lambda, \Omega)\Delta k_i(\lambda), \tag{22}$$

where W_N is the weighting function for the number density $N(z)$ and W_i is the weighting function of Ross-Li model coefficients. The weighting function is the functional of $\delta/\delta N(z)$

and the partial derivatives $\partial/\partial k_i(\lambda)$ of reflectance $R(\lambda, \Omega)$, respectively [2].

According to the derivation from Vountas et al., (2020) [2], the weighting function for the number density W_N is substituted by the weighting function for the aerosol optical thickness W_τ. Taking into consideration the real measurements of a satellite instrument, the variation of the TOA reflectance ΔR can be also expressed as the difference of the measured TOA reflectance R and a TOA reflectance modeled using a priori values for atmospheric and surface reflectance, R_0, thus Eq.[22] can be written as:

$$R(\lambda_j, \Omega_m) = \hat{R}_0(\lambda_j, \Omega_m) + W_\tau(\lambda_j, \Omega_m)\tau + \sum_{i=1}^{3} W_i(\lambda_j, \Omega_m)k_i(\lambda_j) \tag{23}$$

with

$$\hat{R}_0(\lambda_j, \Omega_m) = R_0(\lambda_j, \Omega_m) - W_\tau(\lambda_j, \Omega_m)\tau_0 - \sum_{i=1}^{3} W_i(\lambda_j, \Omega_m)k_{i,0}(\lambda_j), \tag{24}$$

where $j = 1, ..., L$; $m = 1, ..., M$; and L, M are the number of wavelengths and observation directions, respectively. R_0 is the TOA reflection function calculated using a priori values for atmospheric and surface parameters, τ_0 is the a priori AOT and $k_{i,0}$ are the a priori Ross-Li coefficients.

Eq. [23] can be expressed in vector matrix form as follows:

$$\vec{R} = \vec{R}_0 + \mathbf{W}_0\vec{X}. \tag{25}$$

The estimation of the vector of parameters $\vec{X}$ is determining the difference of the L2 norm of Eq.[26]:

$$||\vec{R} - \vec{R}_0 - \mathbf{W}_0\vec{X}||^2 \rightarrow min. \tag{26}$$

The minimization problem in Eq. [25] is solved by Quadratic Programming (QP) approach. The QP method is effective to perform that minimization of the objective function using linear constraints. These constraints can be set by the user. In this study, QP method is used this far with no constraints except for AOT limits $0.01 < \tau < 1.5$ [2]. The inverse problem with respect to AOT, τ and Ross-Li coefficients, k_i, is solved using Eq. [26] iteratively. In iterative approach, values from previous iterations are used instead of a priori information τ_0 and $k_{i,0}$ in Eq.[24], which is only used initially.

5 Methodology

The purpose of the study is to retrieve the AOT from satellite data using SCIATRAN, and evaluate the retrieval algorithm utilized by the radiative transfer model and retrieval model as explained in chapter 4. The AOT is retrieved from multi-viewing and multi-spectral POLDER instrument data on-board PARASOL mission described in chapter 3.1. The retrieval is evaluated by carrying out a global validation against AERONET ground-station measurements described in chapter 3.2. In addition, auxiliary data from Aqua/MODIS instrument mentioned in chapter 3.3 has been used.
The procedure consists of four main work steps. The first work step is to prepare input data POLDER/PARASOL and AERONET for the retrieval and evaluation processes. The data is co-located and pre-processed including geometrical corrections. The second work step is to set up the software package SCIATRAN and perform the retrieval algorithm. In the third work step, retrieval results were validated by creating scatter plots using the AERONET data. Finally, the validation results are evaluated and analyzed to reach a solid assessment of the retrieval algorithm.

5.1 Data Preparation and Preprocessing

A full month (August 2008) dataset of level-1 POLDER data was downloaded from `ftp://ftp.icare.univ-lille1.fr/SPACEBORNE/PARASOL/L1_B-HDF.v1.01/2008/`. The data files are in HDF format and each file represents a complete orbit. One file includes up to 16 directional measurements of the sun-normalized radiance for each of the 9 spectral channels shown in Table 1, angular information of the pixel center (solar zenith angle, viewing zenith, and relative azimuth angles for channel 670P), geolocation information of the pixel center (latitude, longitude, and surface altitude), and Stokes vector components for polarization channels 490P, 670P, and 865P are given. The dataset needs several preprocessing steps before being used within the retrieval algorithm of SCIATRAN. A python tool *h5readpolder.py* was developed to apply the preprocessing and corrections steps, which are discussed below:

- POLDER data is recorded in an integer binary coding format with either 1 or 2 bytes. In order to compute the physical value (PV) for each quantity, the following formula is applied to each binary value (BV) in the scientific dataset (SDS) counts [12]:

$$PV = f \times BV + b, \tag{27}$$

the scaling factor (f) and offset value (b) are provided in each L1-b file for each parameter.

- Data are acquired globally, but measurements over the water are not considered. Because the surface parametrization used in this study has not yet been prepared for water bodies. The water pixels were masked. The mask was applied using the land-sea flag parameter provided in the level-1 file. The parameter equals 0 over water, 100 over the land, and 50 over mixed areas.

- Due to the sequential data query system used by the POLDER/PARASOL instrument, surface targets are observed with slightly varying viewing angles at different spectral channels. The instrument is scanning in 15 spectral/polarized observations[4] which are acquired sequentially. In aerosol optical properties retrieval, the small differences in observation geometry can make significant changes in the results, which will be shown later in chapter 5.1.3. Accordingly, the geometrical correction recommended by POLDER/PARASOL documentation [12] was applied to the data. In the level-1 data product, the viewing zenith angle θ_0 and relative azimuth angle ϕ_0 are provided only for the 670P channel. To derive the angles θ_j and ϕ_j for other spectral channels, the given formulas [28] and [29] are applied to 670P channel angles θ_0 and ϕ_0:

$$\theta_j = \sqrt{(\theta_0 \cos\phi_0 + X_j DV_z C)^2 + (\theta_0 \sin\phi_0 + X_j DV_z S)^2}, \tag{28}$$

and

$$\phi_j = \arctan\left[\frac{\theta_0 \sin\phi_0 + X_j DV_z S}{\theta_0 \cos\phi_0 + X_j DV_z C}\right], \tag{29}$$

If $\theta_0 \cos\phi_0 + X_j DV_z C < 0$, then $\phi_j = \phi_j + 180°$.

The two parameters $DV_Z C = \Delta[\theta_v \cos\phi]$ and $DV_Z S = \Delta[\theta_v \sin\phi]$ are given for each viewing direction in the data file, and X_j is given in the table below:

Channel	443P	490NP	565NP	670P	763NP	765NP	865P	910NP	1020NP
X_j	-6	-4	-2	0	2	3	6	4	-3

Table 3: Parameter X_j values at each spectral channel [12]

[4] the 16th acquisition is to estimate the CCD sensor *dark current* and it is not relevant to angular correction

In parallel, a full dataset of AERONET AOT data was downloaded. The dataset includes AOT measured values at 500nm at all globally existing AERONET stations. The location for each station and ground elevations are provided on the database website and was downloaded from `https://aeronet.gsfc.nasa.gov/Site_Lists_V3/aeronet_locations_v3_2020_lev20.txt`. Even though processed pixels were reduced to only the pixels in the vicinity of AERONET stations, processing time during this study is still too long to complete one orbit analysis. The python tool *h5readpolder.py* carried out the step of co-locating POLDER pixels in a radius of 25 km around the AERONET station to improve statistical representation [2]. The tool used the geolocation information provided within both datasets files; POLDER and AERONET. The tool co-located 133 AERONET stations with POLDER orbits data in August, 2008 shown in (Figure 14). Each station has measured AOT on the same matching days of the POLDER orbit but not necessarily at the same time as POLDER. In contrary to Vountas et al. (2020) which considered a time window of $\pm$15 minutes to average the AERONET measurements, we averaged the measurements temporally within $\pm$ 30 minutes the POLDER acquisition for better statistical representation.

The tool produces a netCDF file for each co-located station as an output. Each file includes only POLDER pixels which are co-located with the AERONET station (Figure 15), in addition to the same AERONET station AOT measurements. These files are used as inputs for the SCIATRAN model to run the retrieval process.

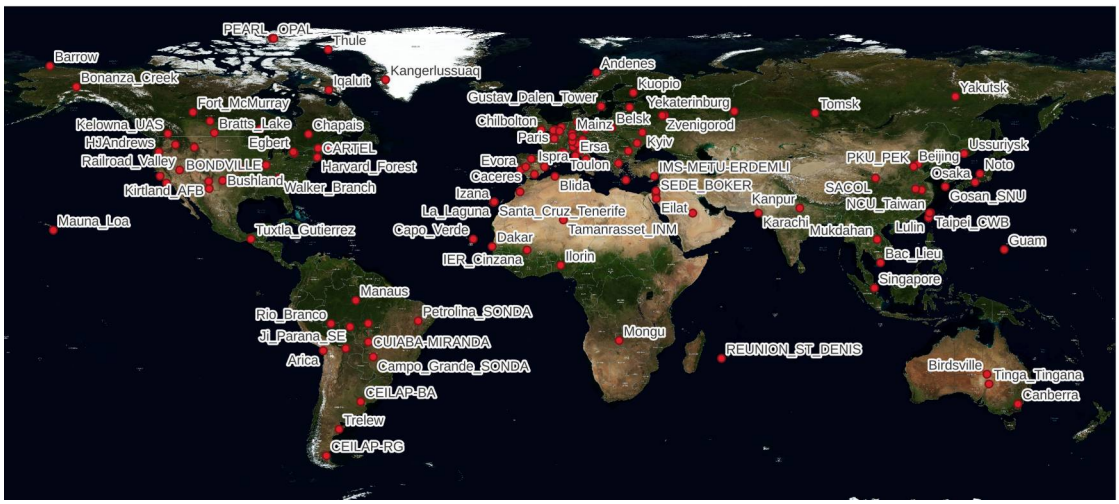

Figure 14: A global map shows the 133 AERONET stations providing co-located data in August 2008 with POLDER. The background map is the blue marble product of the MODIS instrument provided on `https://worldview.earthdata.nasa.gov/`.

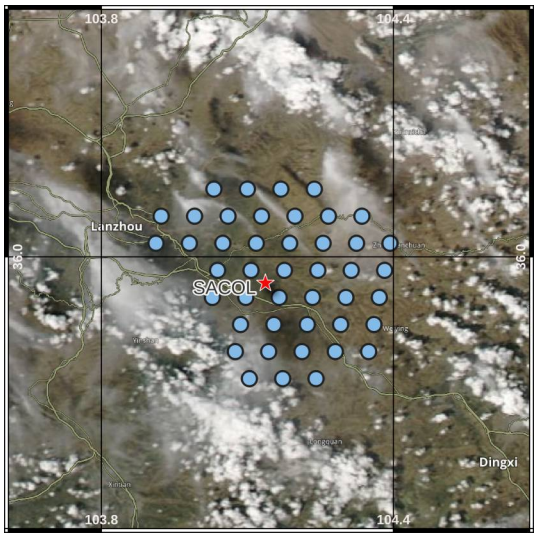

Figure 15: A visualization of a co-located AERONET station (SACOL, China), shown as a red star, with the selected POLDER measured pixels, shown as blue dots, in 25 km radius around the station on 30 August, 2008. The background map is a true color image from Aqua/MODIS on the same day.

5.2 Processing retrieval

The computational resource utilized in this study to run SCIATRAN is the Hypatia high performance computing cluster. Hypatia is based on Intel Xeon Gold processors from the Cascade Lake generation and provided/owned by the institute of environmental physics (IUP), University of Bremen. Hypatia consists of 20 nodes with a total of 640 processor cores, each compute node is equipped with:
- 2 sockets Intel Xeon Gold 6226R CPU with 16 cores each opertated at 2.9GHz for a total of 32 cores per node;
- cache L1 1 MiB; L1I 512 KiB; L1D 512 KiB; L2 16 MiB; L3 22 MiB;
- 768 GB of main memory 24 GB/core, 12x 64GB DDR4 ECC REG 2933;
- 1 Mellanox ConnectX-4 EDR;
- 10 Gbit/sec Ethernet;
- 2 x 240 GB local SSD.

SCIATRAN has been set up to operate for aerosol optical thickness retrieval. As mentioned, the settings in this study are adapted from Vountas et al. (2020). A summary of retrieval settings is given in the table 4.

SCIATRAN produces a package of text files for each pixel. The package includes the retrieved AOT, geolocation information, number of iterations, underlying surface BRDF, and its components (geometrical, volumetric, and isotopic). All pixels output information is collected in one netCDF file for each station to be used later in the validation.

Retrieval mode	Quadratic Programming method Retrieval of AOT and three surface parameters Constraints AOT: 0.01 and 1.5 Constraints surface parameters: none
Aerosol	MODIS-Land parametrization [41] with spherical aerosols Bi-modal log-normal particle size distribution Fine mode: weakly absorbing aerosols Coarse mode: spheroidal dust fraction of 0 or 10% A priori AOT: 0.1
Surface	Ross-Li BRDF model: **Vegetation type** k_{geo} k_{vol} Grassland 0.056 0.041 Cropland 0.012 0.009
Trace gases	Ozone: Gorshelev et al. [42] NO 2 : Bogumil et al. [43]
Climatological database	Trace gas, temperature and pressure profiles taken from SLIMCAT model (Chipperfield, 1999)
Rayleigh scattering	Parameters from Peck & Reeder (1972)
Utilized spectral information	443 nm, 490 nm, 565 nm, 670 nm, 865 nm
Cloud screening	Taken from the level 1 POLDER product.

Table 4: Relevant set up for SCIATRAN for AOT retrieval [2].

5.3 Angular Correction Code

The retrieval process needs sufficient angular accuracy. In consequence, the geometrical correction described previously in chapter 5.1.1 is applied to POLDER data. One more step before performing the retrieval of the whole data is data quality assurance. Different parameters such as viewing zenith and relative azimuth angles are visualized and several plots are created. Figure 16 depicts the relative azimuth angle which is the difference in azimuth between the sun and the satellite directions: $\phi = \phi_s - \phi_v$ where ϕ_v is defined, as ϕ_s, with respect to the North direction. The viewing zenith angle, θ_v, is relative to the local zenith. It may vary between 0° and approximately $75°$ [12].

The data quality assurance step, performed in this study, showed unexpected patterns of the relative azimuth angles of POLDER measurements (Figure 17.a). Further analyzing of the the developed code revealed a software error. This mistake overwrites the values of the angles in the third quadrant of a polar plot (Figure 17.a) distorting the angular patterns as shown in the figure. The corrected code leads to an expected angular pattern seen in figure 17.b. The figure depicts the observation geometry for the selected pixel (36.138, -84.428). The pixel is located in the vicinity of Walker Branch station on the 23rd of August, 2008.

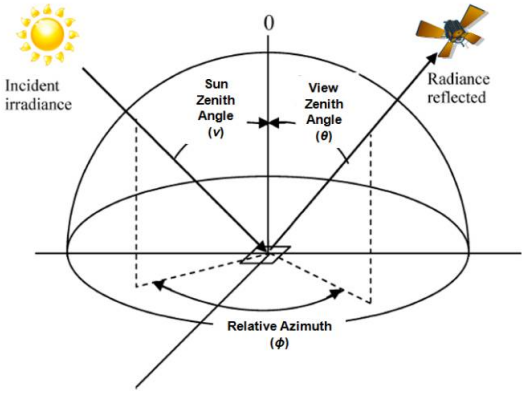

Figure 16: Illumination and viewing angles: solar zenith angle v, viewing zenith angle θ, and relative azimuth angle ϕ (McCamley, 2014) [44] .

To investigate the geometry effect on the level-1 data output quality, SCIATRAN was run for a subset of the data, including the previously selected pixel, before and after correcting the problem. Figure 18 depicts 14 values of the modeled top of atmosphere (TOA) reflectance deviation from the POLDER measured TOA normalized reflectance for the previously selected pixel. The modeled values using corrected data, in green bars, show much less deviation than the modeled values using problematic data in red bars.

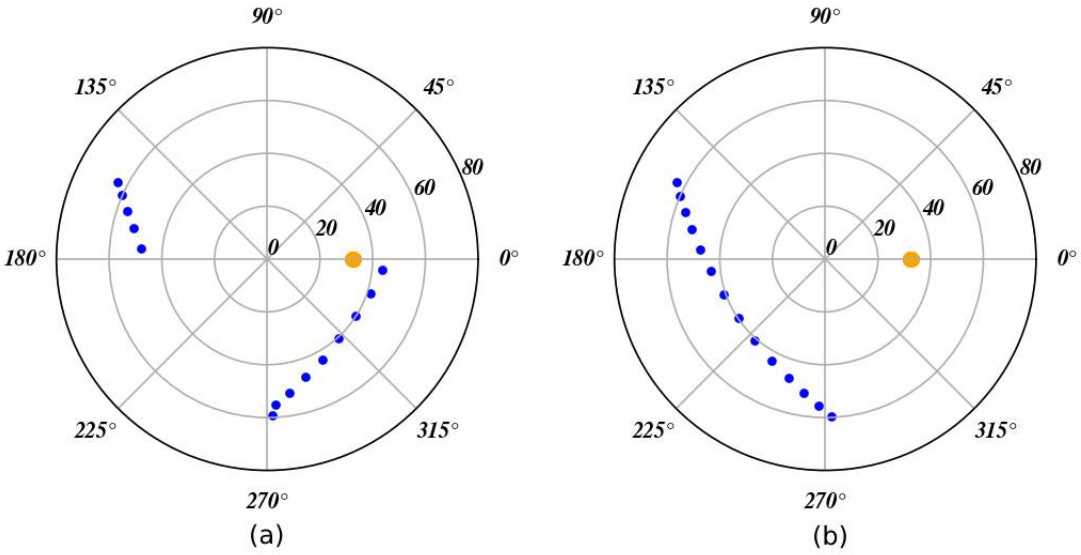

Figure 17: The sun position at zero in orange, and 14 measurements angles in blue. The relative azimuth angle on the radial axis relative to the sun and the viewing zenith angle on the theta axis. (a) problematic data and (b) corrected data.

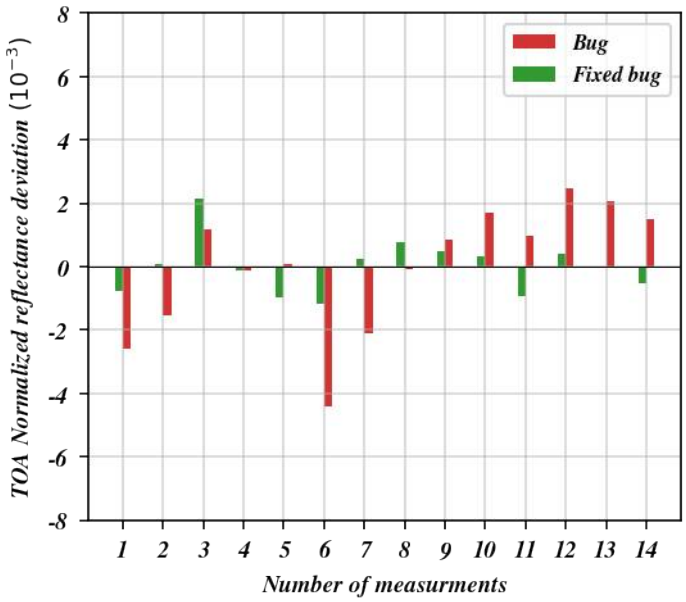

Figure 18: SCIATRAN modeled TOA reflectance deviation from the POLDER measured TOA refelctance at 565nm channel for the selected pixel (36.13889, -84.428734), in the vicinity of Walker Branch station on 23rd of August, 2008. Problematic data shown with red bars and corrected ones in green.

5.4 Validation strategy

In this study, the measured AOT values from the AERONET ground stations have been used to validate the retrieval of aerosol optical thickness from the POLDER/PARASOL dataset. The AERONET measurements were temporally averaged $\pm$ 30 minutes within the POLDER acquisition time. The retrieved AOT using SCIATRAN were spatially averaged in a 25 km radius around the AERONET ground station [2]. A scatter plot for both averaged values was created to evaluate the retrieval. The AOT retrievals were classified from the scatter plot into well-estimated, underestimated, or overestimated: If the retrieved value is within the accepted range[5] in Eq. 30, it is considered **well-estimated** [46].

$$\Delta\tau = \pm 0.7 \times \tau_{aeronet} \tag{30}$$

A detailed investigation of outliers (under - or overestimations) was carried out using auxiliary data, described in chapter 3.3, as explained in (Figure 20). The investigation aims to explore the cause of the outliers, whether the reason is an algorithm inadequacy or other limitations related to the used datasets, such as cloud contamination, are the cause or both

[5] In this study, a less rigid range than in Remer et al. (2005) ws adopted, due to the smaller number of available pixels.

reasons play a role. The POLDER cloud mask (CM) was evaluated for each station using the Aqua/MODIS cloud fraction product, described in chapter 3.3.2. The evaluation is done based on the range of cloud fraction (CF) values where the majority of co-located pixels are acquired (Table 5). For example, Figure 19 shows the co-located pixels in the vicinity of the Tamanrasset INM AERONET station superimposed over the color coded MODIS cloud fraction values. Each POLDER pixel is assigned a flag as ”Good”, ”Fair”, or ”Poor” according to the co-located MODIS cloud fraction value range (Table 5). The flag which acquires the largest number of occurrences is used to make the subsequent decision process (Figure 20). In Figure 19 the majority of pixels are within the MODIS CF value range 0-25% which helps us to identify the POLDER CM as ”Good”. Another flag ”Clear” is used in case of completely clear sky (CF 0%). In some cases, when the scene is very cloudy (CF > 75%) the POLDER CM screens most of the pixels efficiently with the 25km radius: Only very few pixels are co-located, leading to mis-estimation of AOT due to insufficient statistical representation.

MODIS (CF) range	POLDER (CM) performance
0% - 25%	Good (G)
25% - 50%	Fair (F)
> 50%	Poor (P)

Table 5: POLDER cloud mask (CM) evaluation using MODIS cloud fraction (CF) dataset.

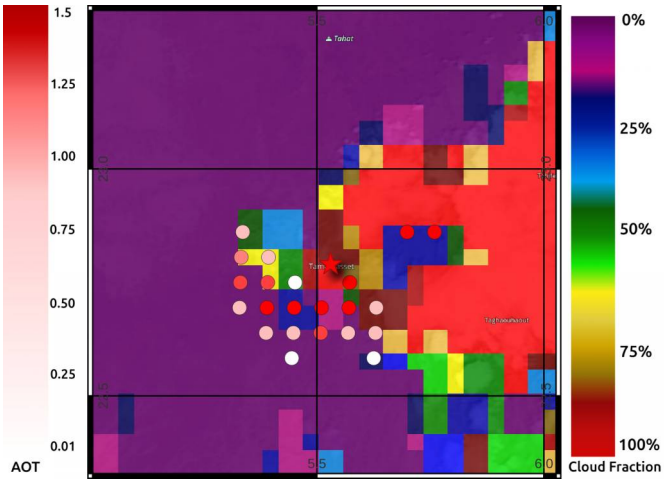

Figure 19: Co-located pixels, in the vicinity of the Tamanrasset INM station, plotted over the cloud fraction layer for POLDER cloud mask evaluation.

The investigation scheme is done as detailed in Figure 20 for all measured days and stations. Results and analysis are presented in chapter 6 and the appendix. As shown in (Figure 14), 133 stations were co-located. To avoid redundancy, the stations were carefully shortlisted to 13 stations (Table 6). The shortlist is well distributed globally based on land cover type, and surrounding environment (Figure 21). Various surrounding environments

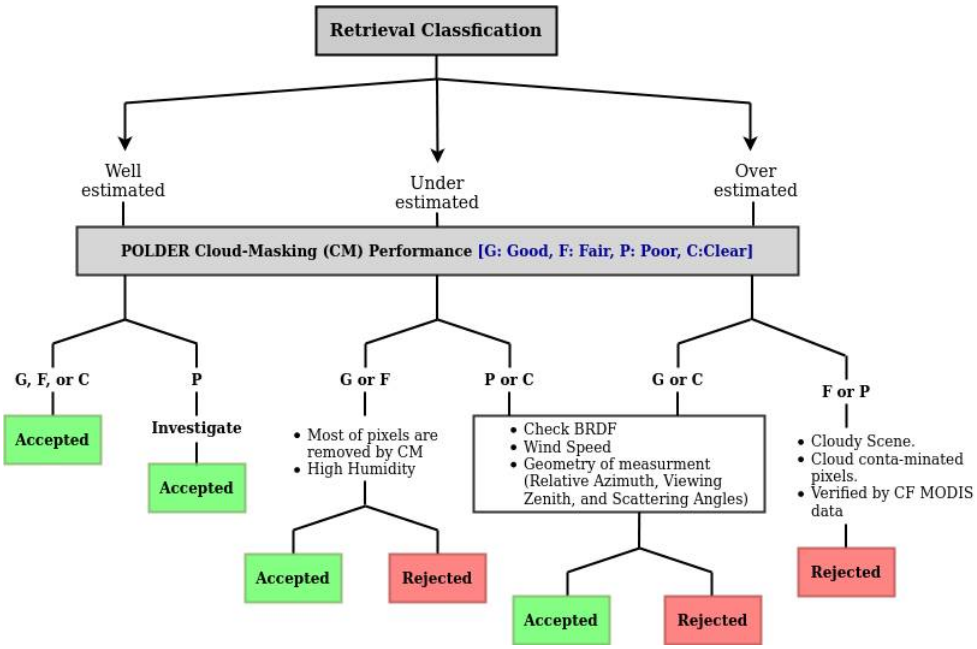

Figure 20: Retrieval evaluation scheme

are selected, including tropical forests, Sahara, and mega cities. Land cover types also are carefully selected to represent various types like vegetation, forests, cropland, grassland, desert, and urban covers. Furthermore, additional constraints were applied to the retrieved results to ensure that sufficient quality could be achieved. In particular, all pixels having an AOT value < 0.05 or were retrieved after more than twelve iteration steps were not considered in the validation.

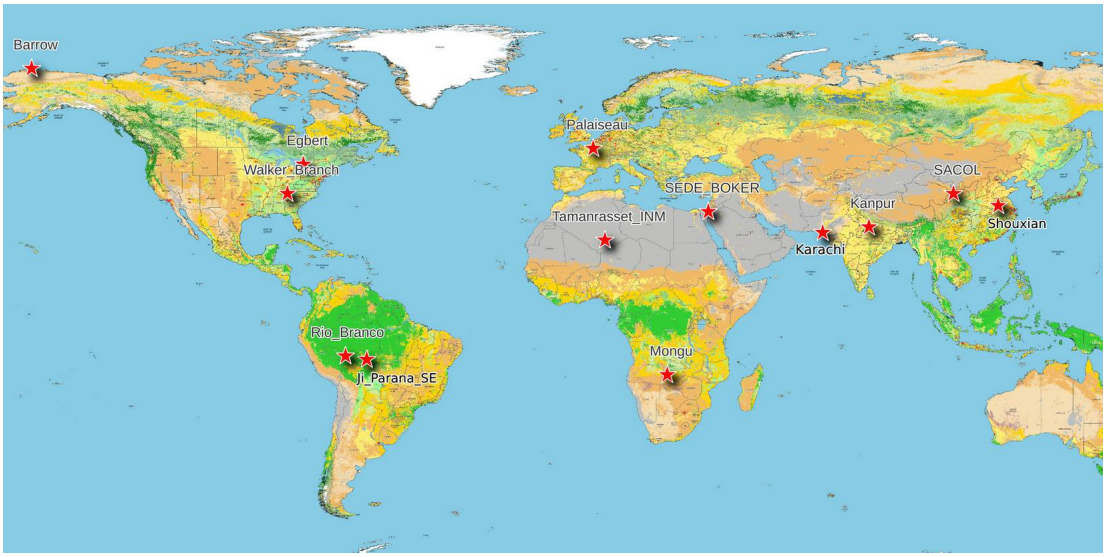

Figure 21: Map of shortlisted stations over MODIS land cover type data

Shortlisted Stations			
Station name	Longitude	Latitude	Land cover type
Barrow	-156.66	71.312	Grassland, snow cover and wetlands
Egbert	-79.781	44.231	Cropland and vegetation
Ji Parana SE	-61.851	-10.934	Savannas
Kanpur	80.231	26.512	Urban and cropland
Karachi	67.135	24.945	Urban and open shrublands
Mongu	23.1508	-15.253	Grasslands
Palaiseau	2.215	48.711	Urban and croplands
Rio Branco	-67.869	-9.957	Urban and savannas
SACOL	104.13	35.946	Grasslands
SEDE BOKER	34.782	30.855	Barren and Desert
Shouxian	116.78	32.558	Cropland and Vegetation
Tamanrasset INM	5.53	22.79	Barren and desert
Walker Branch	-84.287	35.958	Deciduous forests and savannas

Table 6: Shortlisted stations table

6 Results

At each station, SCIATRAN-POLDER AOT retrievals have been spatially averaged within a 25 km radius around the AERONET station at the center. AERONET measurements have been temporally averaged ± 30 minutes within the POLDER acquisition time for all available days. The averaged AOT values were plotted in a scatter plot to evaluate the level of agreement (Figure 22). The scatter plot shows little correlation between the measured and retrieved AOT values with correlation coefficient $R = 0.403$. The value range which is considered here as ”well-estimated” ,as explained in chapter 5.2, is shown in Figure 22 as gray dashed lines. The result of a linear regression of both datasets is shown as black dotted line (the regression parameters are shown in the lower left of Fig. 22).

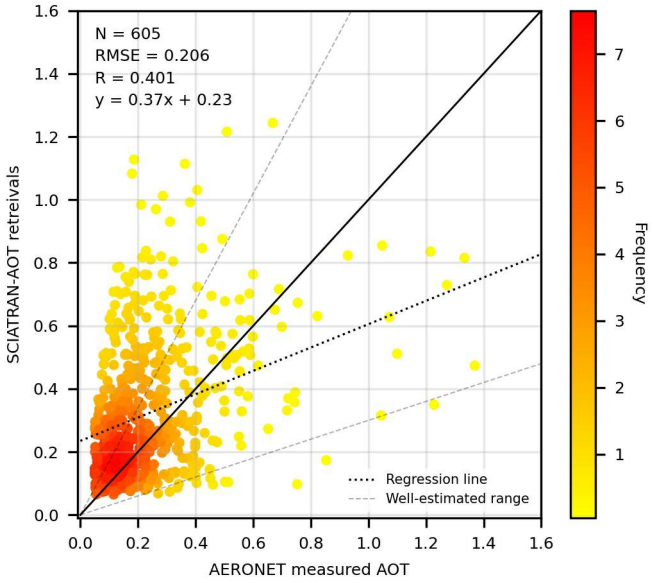

Figure 22: Density scatter plot of temporally averaged AERONET AOT and spatially averaged SCIATRAN AOT for all 133 co-located stations (Full dataset) for all available days. The dotted black line is the best fitting line, the solid line denotes 1:1 line, and the gray dashed lines determine the envelope of the well-estimated retrievals.

Many retrieved AOT values are misestimated showing significant disagreement between both datasets. Most of the misestimated values are overestimation. To thoroughly understand the retrieval results, we examined the outliers to identify the reason behind the overestimation of AOT values retrieved by SCIATRAN. We applied the retrieval evaluation scheme (Figure 20) to the shortlisted stations (Table 6). Figure 23 shows a scatter plot similar to Figure 22, but for the shortlisted stations only. The scatter plot still illustrates a poor correlation coefficient ($R = 0.479$) between both datasets, which is similar to the correlation coefficient value of the full dataset. Thus it is expected that the shortlisted stations are well representing

the full dataset and not biasedly selected.

On the next few pages, the evaluation scheme (Figure 20) is used to examine the reason(s) for each shortlisted station individually. When there is a clear reason for a failed SCIATRAN-AOT retrieval it is discarded from the scatter plot. For the purpose of identification of reasons of poor retrieval quality a scatter plot is created for each station. The scheme starts with evaluating the retrieval results into well-estimated, underestimated, and overestimation according to the expected error range explained in chapter 5.2, followed by evaluating the POLDER cloud mask according to the method described in the same chapter. The scheme's rejection decision does not consider intrinsic deficiencies of the algorithm. For instance, if the assumed a priori aerosol type is not fitting to the one which was prevailing during measurements, then mis-estimation of AOT is expected. But if the retrieval result is influenced by extrinsic factors such as clouds, the scheme rejects the retrieval output. The scheme decisions highlight inferior retrievals, which are pointing to important sources of possible improvements. Both intrinsic and extrinsic factors are discussed in detail below in this chapter.

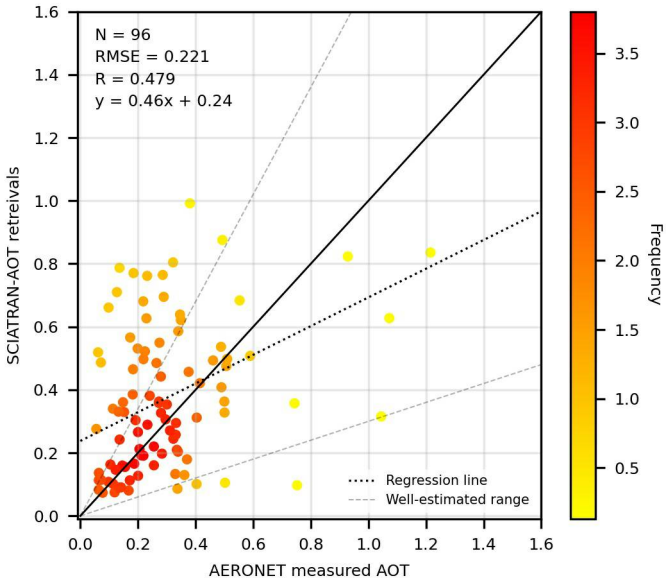

Figure 23: Density scatter plot of temporally averaged AERONET AOT and spatially averaged SCIATRAN AOT for the shortlisted stations for all available days. The dotted black line is the regression line, the solid line denotes 1:1 line, and the gray dashed lines determine the envelope of the **well-estimated** retrievals.

6.1 Residual Cloud Cover Effect

Clouds are often bright, white, cold objects and located higher than the Earth's surface. In fact, clouds sometimes do not satisfy these characteristics. Clouds could be less bright, warm or very close to the surface, as a result, cloud masking algorithms may fail to screen them based on the above defined properties. POLDER cloud mask (CM) scheme, described in chapter 3.1.2, is the only cloud mask considered in this study. POLDER CM is limited and not sufficient for thin, low and patchy clouds [16]. Visual inspection using Aqua/MODIS true color images revealed clouds in some scenes are missed and not masked. Clouds are exhibiting large TOA reflectance in the same spectral channels range (443 nm, 490 nm, 565 nm, 670 nm, 865 nm) utilized in the SCIATRAN-AOT retrieval process (Figure 24). The large reflectance influences the retrieval process leading to overestimation AOT values. The overestimation due to the clouds are found at several shortlisted stations:

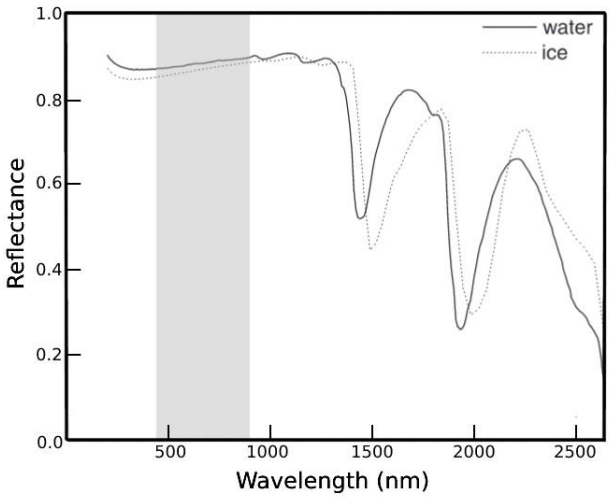

Figure 24: Reflectance of the main components of clouds, showing spectral dependence of cloud reflectance. Retrieval spectral range in this study is shaded in gray. (after Kokhanovsky, 2004) [45]

Walker Branch (84.287 W, 35.958 N) is an AERONET station located in North America and surrounded by vegetation land cover (Fig. 25, right). A scatter plot was created for Walker Branch (Fig. 25, left), and nine days of AERONET measurements could be extracted in the same temporal window of POLDER overflight time (Table 7). Each day has been evaluated using the retrieval evaluation scheme. True color images of the station in the corresponding days show cloud contaminated scenes (Fig. 26 and 27). As stated before, the low clouds are hardly detected and masked by POLDER CM. Therefore, four days of data were removed from the analysis. In Table 7, several days were rejected, even if they exhibited "Fair" POLDER CM values because of poor statistics.

Walker Branch			
Land Cover and Environment: Deciduous Forests/ Savannas			
Date	SCIATRAN	POLDER CM	Notes
08	Over	Fair	Low and patchy clouds
09	Over	Fair	Low and patchy clouds
11	Well	Clear	NONE
14	Well	Fair	None
15	Over	Fair	Thin clouds
18	Over	Fair	Thin clouds
23	Well	Clear	NONE
30	Well	Good	NONE
31	Well	Good	NONE

Table 7: Retrieval evaluation of nine extracted days in August 2008 at Walker Branch station. Rejected retrievals are colored in gray.

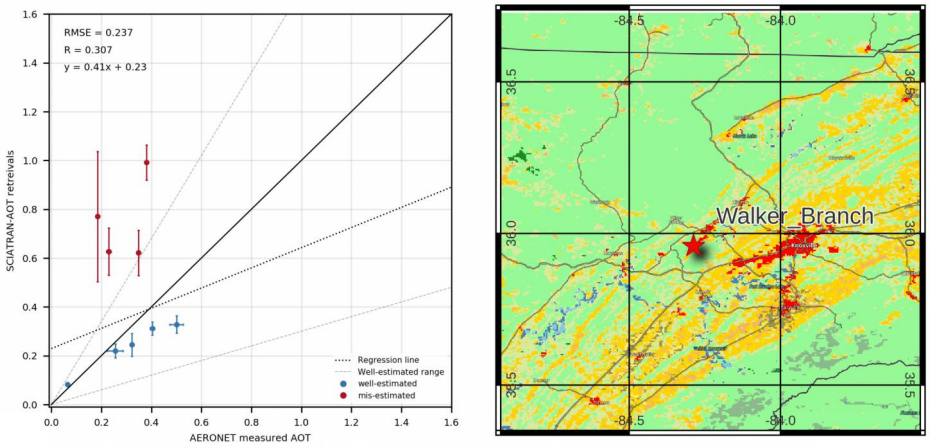

Figure 25: Left: Scatter plot of extracted days, Right: Land cover type of Walker Branch environment

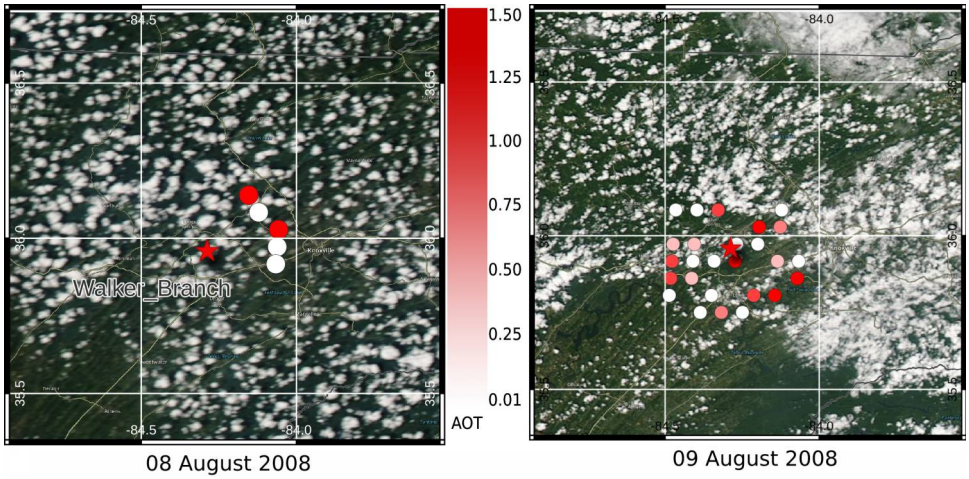

Figure 26: True color images of rejected days at Walker Branch station.

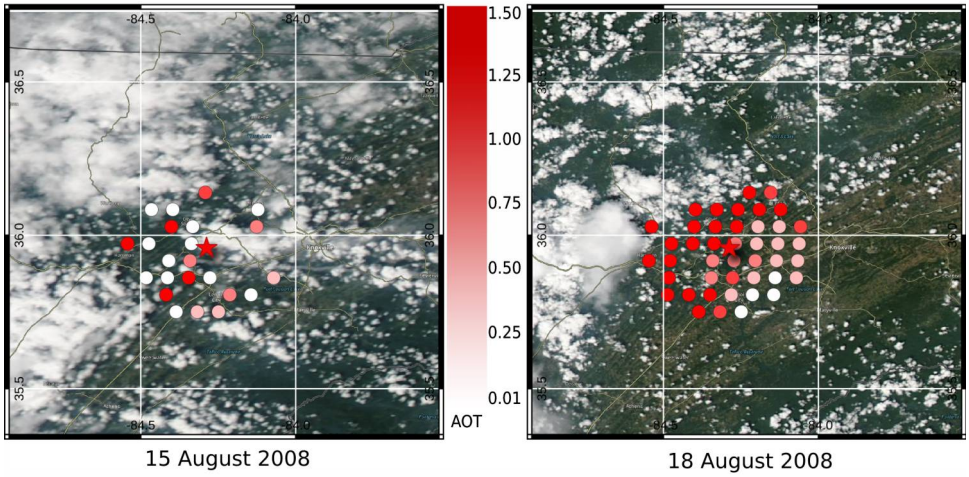

Figure 27: True color images of rejected days at Walker Branch station.

Tamanrasset INM station is another example of cloud effect on the retrieval process output quality. Tamanrasset is located in Sahara (5.53 E, 22.79 N). The station is surrounded by desert/barren land cover (Figure 28, right). Although the Ross-Li BRDF model utilized in this study is developed mainly for vegetation land cover, the scatter plot for 12 extracted days shows surprisingly good agreement for most of these days (Figure 28, left). The evaluation scheme identified the days when overestimated AOT values were found from SCIATRAN retrievals as cloud contaminated scenes based on MODIS true color images product (Figure 29) which were not identified by POLDER CM. The full scheme evaluation is shown in (Table 8). Accordingly, an improvement of the cloud mask would lead to clearly better retrieval results even over desert land cover in Tamanrasset INM station case.

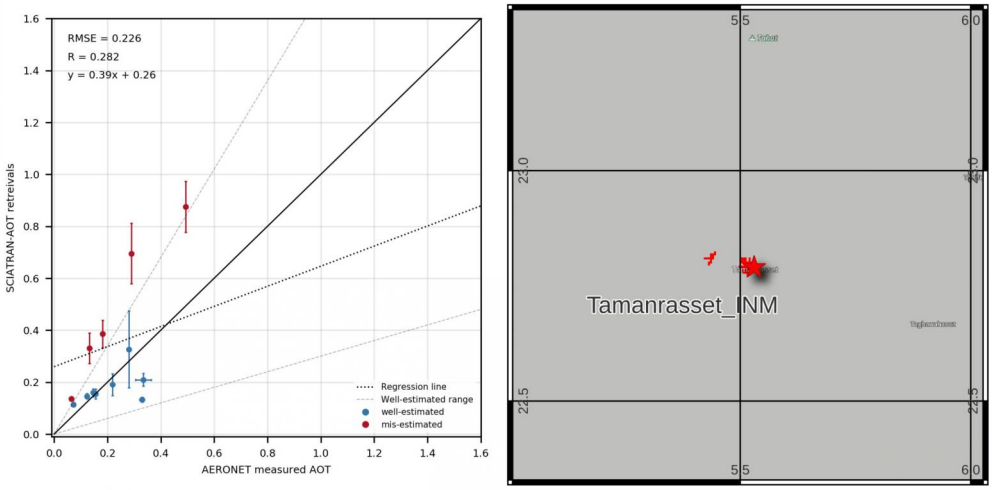

Figure 28: Left: Scatter plot of extracted days, Right: Land cover type of Tamanrasset INM environment

Tamanrasset_INM			
Land Cover and Environment: Barren/Desert			
Date	SCIATRAN	POLDER CM	Notes
07	Well	Good	Low and patchy clouds
08	Well	Good	NONE
12	Well	Clear	NONE
14	Well	Good	NONE
15	Well	Clear	NONE
17	Over	Clear	NONE
19	Over	Good	Low and patchy clouds
21	Over	Good	Low and patchy clouds
23	Well	Good	NONE
24	Over	Fair	Cloudy scene
26	Over	Fair	Low and patchy clouds
28	Well	Clear	NONE
31	Well	Good	NONE

Table 8: Retrieval evaluation of 13 extracted days in August 2008 at Tamanrasset INM station. Rejected retrievals are colored in gray.

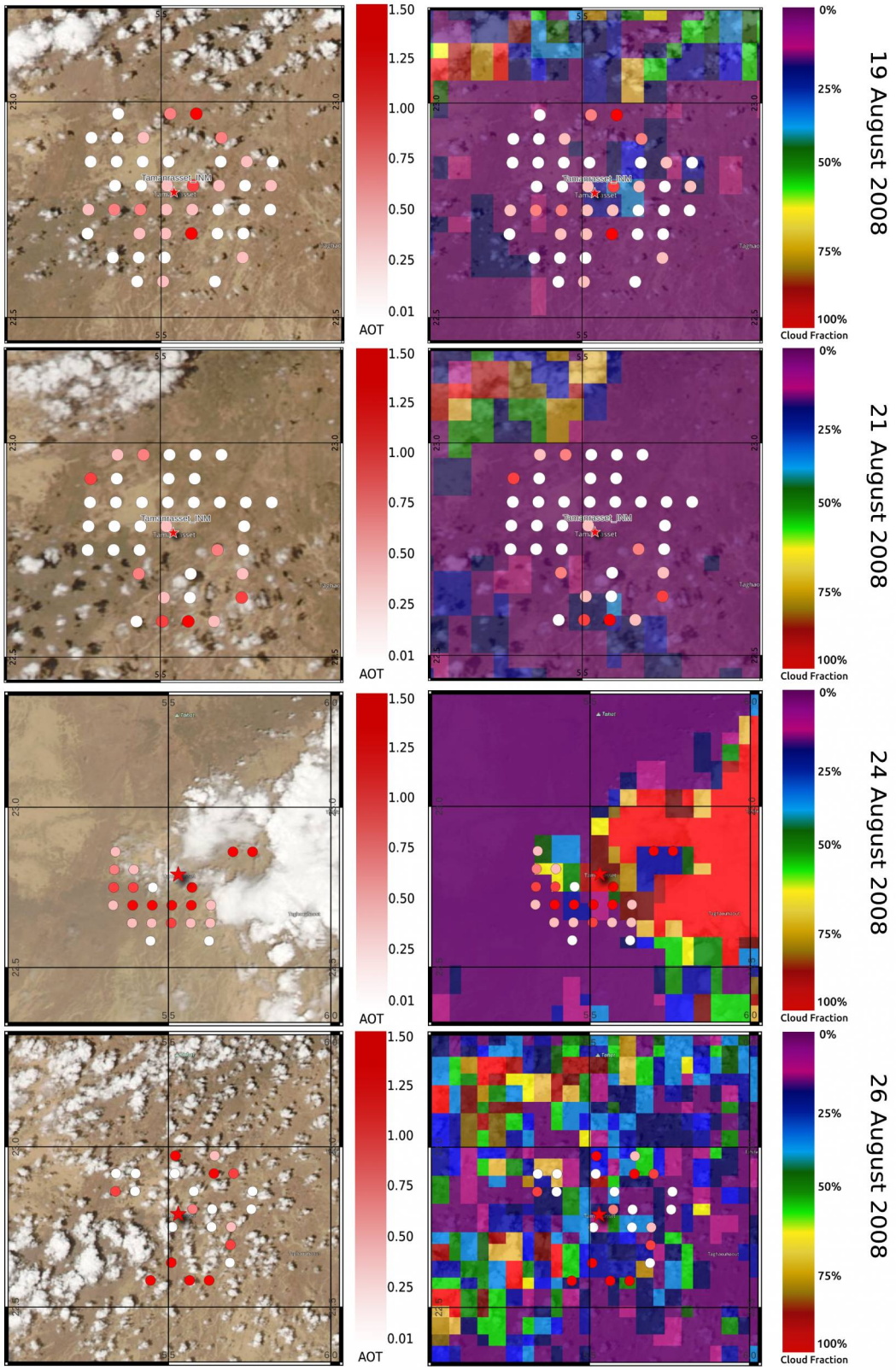

Figure 29: Retrieved AOT over Tamanrasset INM AERONET station. Left Column: MODIS true color images. Right Column: color coded MODIS cloud fraction values

6.2 Quickly changing conditions over stations

As explained in chapter 5.1.1, the AERONET station data is temporally averaged ±30 minutes within the POLDER acquisition time. A temporal window of one hour might lead to large disagreement between AERONET measurements and SCIATRAN AOT retrievals if the conditions during this period change significantly. If, for instance, during this hour of time dust, smoke or other aerosol laden plumes are generated or driven into the direction of the station the AERONET AOT might change by a factor of two or more whilst SCIATRAN retrievals were not exactly, temporally co-located and will thus not be able to detect such changes.

Mongu AERONET station is a good example for such a disagreement due to quickly changing conditions. The station is located in Zambia (23.150 E, 15.253 S). The land cover of the surrounding area is dominated by Grassland (Figure 30, right). The scatter plot (Figure 30, left) depicts very good agreement for most of extracted days. The results applying the evaluation scheme are shown in Table 9. One day, 7. Aug. 2008, was rejected due to the presence of low and patchy clouds, as depicted in the upper row of Figure 31. The MODIS true color image of the underestimated day (29 August 2008) shows heavy smoke plumes in the scene depicted in the lower row of Figure 31. The dry season in the region lasts from mid-April to October. The middle to late period of the dry season is known for frequent bushfires caused by anthropogenic or natural factors [47]. The day under investigation falls in the same period commonly known for bushfires. Another product of MODIS is the fires and thermal anomalies product, it confirms the occurrence of bushfires in the region. The lower left panel of the Figure 31 shows each wildfire event as an orange dot. The quickly moving plumes could cause significant temporal changes leading to under-estimation of AOT values relative to AERONET measurements. Day (27 August 2008) has the same conditions and it is underestimated but still within the accepted range of retrieved AOT values. Consequently, it was marked as accepted.

Mongu			
Land Cover and Environment: Grasslands			
Date	SCIATRAN	POLDER CM	Notes
07	Over	Poor	Low and patchy Clouds
09, 11, 13, 14, 16, 18, 20, 21, 23, and 25	Well	Clear	NONE
27	Well	Poor	Smoke plumes
29	Under	Poor	Smoke plumes
30	Well	Clear	NONE

Table 9: Evaluation of 14 retrievals in August 2008 at Mongu station. Rejected days are in gray.

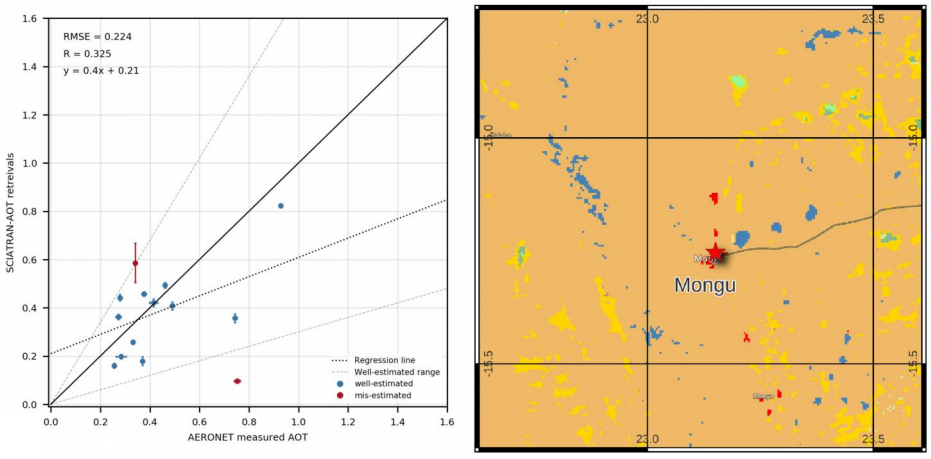

Figure 30: Left: Scatter plot of extracted days, Right: Land cover type of Mongu environment

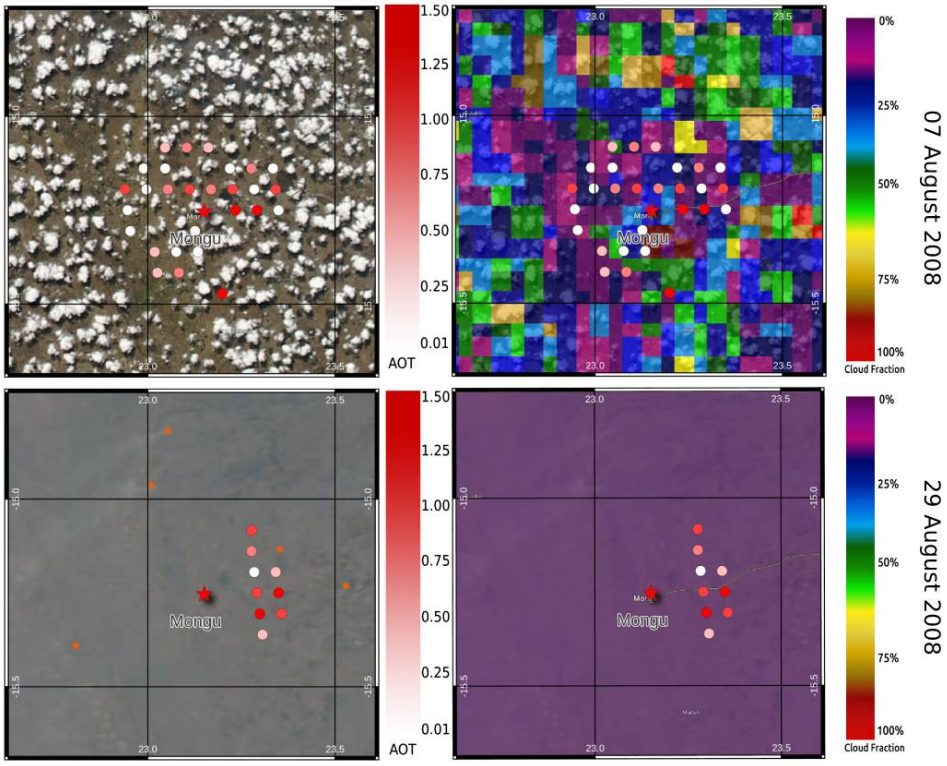

Figure 31: Retrieved AOT over Mongu AERONET station. Left Column: MODIS true color images, and bushfire events are represented as orange dots. Right Column: color coded MODIS cloud fraction values

Another case of such quickly changing conditions can be found at SEDE BOKER AERONET station. The station which is located in Negev desert (34.782 E, 30.855 N) is discussed in detail in the next section 6.3. But the case of the day (28 August 2008) is worth mentioning where a dust storm is seen in the MODIS RGB image (Figure 33).

6.3 Stations over bright surfaces

In this study, the Ross-Li BRDF model, described in chapter 4.2, is used to characterize surface reflectance. Be reminded, that the Ross-Li BRDF model is mainly developed to model reflectance from vegetation surfaces [33]. Consequently, Ross-Li model's limitations are expected to be observed over bright surfaces like desert.

SEDE BOKER AERONET station (34.782 E, 30.855 N) which is located in Negev desert is an example. The station is characterized by a barren/desert land cover (Figure 32, right). Twelve days of POLDER data were extracted in August 2008. The retrieved AOT using SCIATRAN is compared to AERONET in scatter plot (Figure 32, left). The correlation coefficient $R = 0.324$ shows poor parity with ground measurements. After detailed examination using the evaluation scheme (see Table 10), the misestimated days are anticipated as a result of the Ross-Li BRDF model limitations.

The day (28 August 2008) which is discussed previously in the context of quickly changing conditions could give another insight. The scene shows a strong dust storm all over the region and extended over the Mediterranean sea (Figure 33). The dust model used in the retrieval settings (Table 4) describes the coarse mode of aerosol as spheroidal dust with a fraction of 10%. Tuning the dust model to fit the conditions of the station could significantly enhance the retrieval over SEDE BOKER station. Using the evaluation scheme, described in chapter 6, the misestimated days were marked as rejected only if the retrieval result was affected by factors independent from the retrieval algorithm used in this study. As the misestimated days of SEDE BOKER are due to Ross-Li model limitations or dust model settings, the days were not marked as rejected.

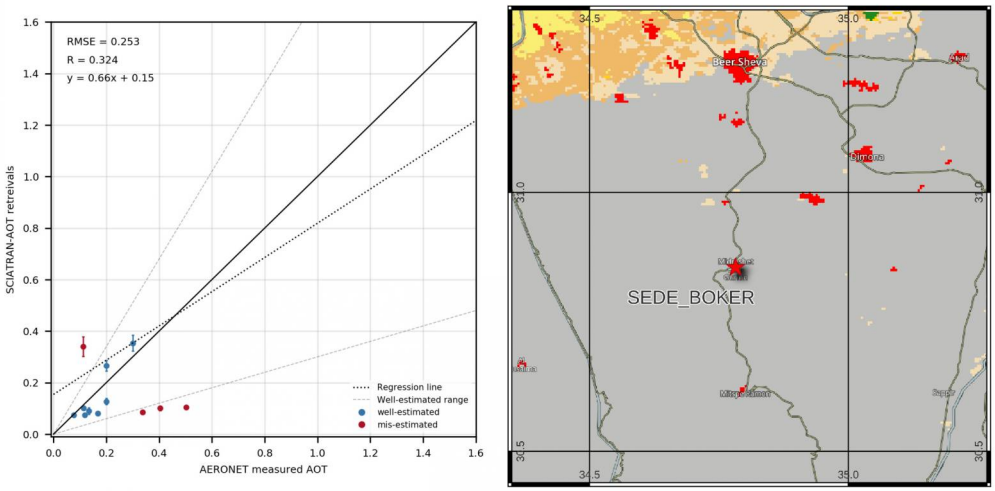

Figure 32: Left: Scatter plot of extracted days, Right: Land cover type of SEDE BOKER environment

SEDE_BOKER			
Land Cover and Environment: Barren/Desert			
Date	SCIATRAN	POLDER CM	Notes
07	Well	Clear	NONE
09	Well	Clear	NONE
11	Over	Clear	NONE
12	Well	Clear	NONE
14	Well	Clear	NONE
16	Well	Clear	NONE
18	Well	Clear	NONE
19	Under	Clear	NONE
25	Well	Clear	NONE
27	Well	Clear	NONE
28	Under	Clear	NONE
30	Under	Clear	NONE

Table 10: Retrieval evaluation of 12 extracted days in August 2008 at SEDE BOKER station. Rejected retrievals are colored in gray.

Figure 33: Dust storm seen over the whole region of SEDE BOKER station

6.4 Presumable aerosols above clouds

Most satellite retrievals of aerosols, like the retrieval in this study, are restricted to the cloud-free regions. In the present study limitations of the operational POLDER CM have been shown. Several SCIATRAN retrievals were having good agreement with AERONET data, although, several cases of missed clouds were present in the POLDER CM. This unexpected good agreement could have been due to high wind speeds and a corresponding change in cloud fraction during one hour of temporal co-location window. Such high wind speeds, however, were not observed within this study. Thus, another probable interpretation is the presence of aerosols above clouds. Aerosol above clouds have been identified as one of the leading source of uncertainty in measuring the global source of aerosol burden [48]. The retrieval algorithm could consider the clouds as a bright surface and retrieve the AOT above the clouds, specially low clouds. Shouxian AERONET station in China (116.781 E, 32.558 N) is a case where presence of aerosol above clouds is probable. The station is located within croplands close to a big urban community of Hauinan city (2.5 millions population). It is worth mentioning, that the city is a main coal producer in China. The station provides data only for four days in August 2008. The four days show good agreement even with two days of them (06 and 24 August 2008) where CM is marked as ”Poor” (Table 11) and obvious cloud contamination is seen in the MODIS true color images (Figure 35). Extending the retrieval algorithm to consider the aerosol above clouds can be possible.

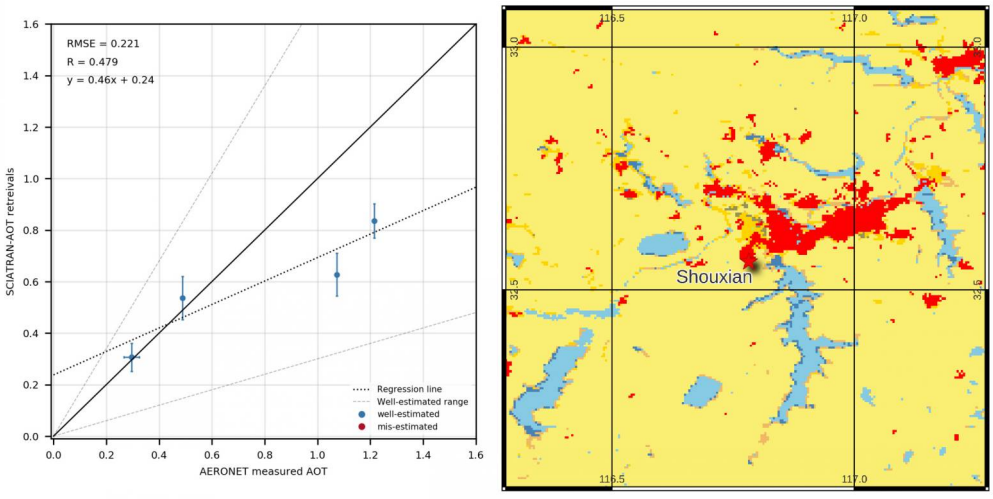

Figure 34: Left: Scatter plot of extracted days, Right: Land cover type of Shouxian environment

Shouxian			
Land Cover and Environment: Cropsland/Vegetation			
Date	SCIATRAN	POLDER CM	Notes
06	Well	Poor	Probable aerosol above clouds
09	Well	Good	Heavy aerosol load
13	Well	Good	Heavy aerosol load
24	Well	Poor	Probable aerosol above clouds

Table 11: Retrieval evaluation of 4 extracted days in August 2008 at Shouxian station. Rejected retrievals are colored in gray

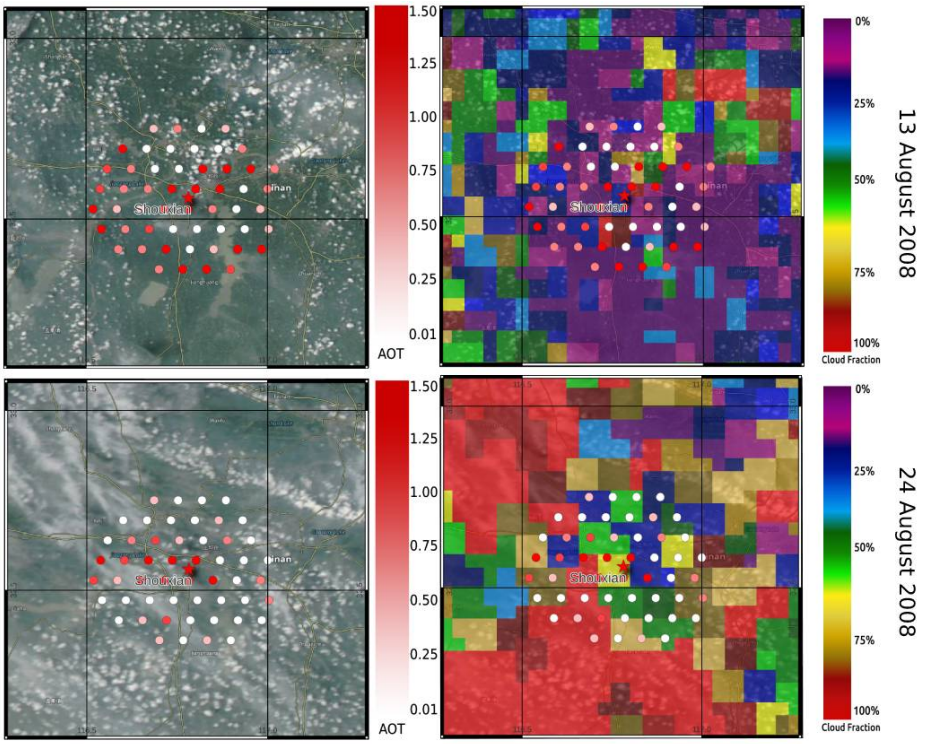

Figure 35: Retrieved AOT over Shouxian AERONET station. Left Column: MODIS true color images. Right Column: color coded MODIS cloud fraction values

6.5 Free-clouds and stable conditions

The previously mentioned results show that outliers are mostly due to cloud residuals or unstable conditions (e.g. Wildfires or Dust storms). The rejected data points using the evaluation scheme are discarded and only the accepted data points using the scheme are plotted in a scatter plot. Figure 36 shows that scatter plot of the SCIATRAN-AOT retrievals within free-clouds and stable conditions. The retrievals show very good agreement and correlation coefficient $R = 0.856$.

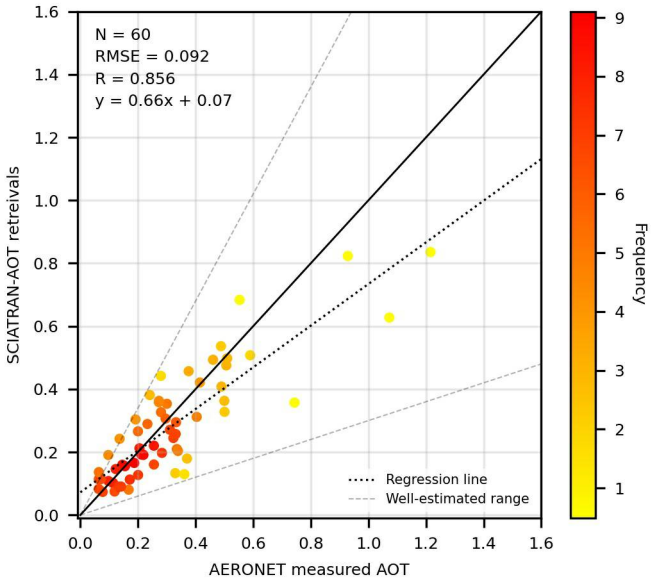

Figure 36: Density scatter plot of SCIATRAN-AOT retrievals and AERONET-AOT measurements within free-clouds and stable conditions. The dotted black line is the regression line, the solid line denotes 1:1 line, and the gray dashed lines determine the envelope of the **well-estimated** retrievals.

7 Conclusions and Outlook

This master thesis has successfully implemented the novel high-quality Aerosol Optical Thickness (AOT) retrieval algorithm introduced by Vountas et al. (2020) [2]. The implementation was followed by detailing a strategy for evaluating data quality. Finally the validation step demonstrated to large extent good agreement with the reliable ground-based AERONET measurements.

The aforementioned algorithm utilizes unpolarized multi-spectral and multi-viewing satellite data. The Ross-Li BRDF [6] model was used to parameterize the direction surface reflectance. The developed retrieval solves the minimization problem using the quadratic programming (QP) approach. Linear constraints being the central assets of the QP approach can be set by the user. But almost no constraints were set in this study for the surface parameters and the AOT retrieval, apart from a relaxed constraint which assumes that the retrieved AOT at $0.5\mu m$ is larger than 0.05 and smaller than 1.5. The retrieval algorithm was performed successfully using the radiative transfer and retrieval model SCIATRAN. AOT and BRDF parameters were retrieved from level-1 sun normalized radiance measured by the POLDER/PARASOL instrument for one month of data (August 2008). The global ground-based network of sun photometers AERONET (AErosol RObotic NETwork) has a very small expected error of approximately 0.01 - 0.02 AOT [13], which makes its measurements very accurate and reliable. Thus, the retrieved AOT values were validated by finding those co-located within a radius of 25 km around ground-based measurements from AERONET [2]. Due to the detailed evaluation scheme and to avoid redundancy, the total 133 co-located stations were shortlisted, leading to 13 representative stations (see Table 6 in chapter 5.4).

From a careful analysis it could be shown that under cloud-free and stable conditions, the SCIATRAN-AOT retrievals demonstrated very good agreement with AERONET-AOT measurements. The correlation coefficient $R = 0.856$ (Figure 36) confirms the good agreement of the results. Also, the retrievals can be seen as almost homogeneous in the vicinity of AERONET stations in the MODIS true-color image shown in the results chapter 6 and appendix. **An improved cloud mask** with respect to low clouds and optically thin clouds masking will help to overcome the limitations of the operational POLDER cloud mask. The extended cloud mask would provide the necessary clear sky conditions leading to significantly improved AOT values .

Non-stationary conditions, especially temporally *rapid* changes, such as wildfires and dust plumes are influencing the validation strategy as shown in chapter 5.2. One of the

[6] Bidirectional reflectance distribution function.

influencing factors is the large time window which is set for averaging AERONET-AOT measurements. Thus, in such cases, **a smaller temporal window** would have been beneficial to avoid a bias due to non-stationary conditions. However, a general, i.e. global, reduction of the temporal window would been problematic because it would have lead to poorer statistics, because of less pixels being averaged over the station. Improved agreement and therefore a larger correlation coefficient can be obtained by **fine-tuning and adapting** parameters of the dust model according to the environment.

Surprisingly, the study revealed good and unexpected results modeling the surface reflectance using the Ross-Li BRDF model over bright surfaces such as desert, even though the latter was mainly developed for vegetation surfaces. Tamanrasset INM station in Sahara is a good example where 8 out of 9 retrievals under cloud free conditions were within the accepted range of expected error (see Table 8 and Figure 28 in chapter 6.1). Consequently, **an extensive study** of retrievals over bright surfaces using the Ross-Li model and validation of the surface parameters could be helpful to understand this behavior. Additionally, setting constraints for the surface parameters can provide supportive surface modeling and description, which could lead to improved retrievals.

A python tool was developed to preprocess POLDER level-1b data and co-locate them with AERONET stations. After fixing an error in the code of the angular correction functions used for POLDER level-1b data as explained in chapter 5.3, the study showed that the retrieval results were sensitive to the provided angular information (see Figure 18) in the same chapter). Accordingly, **a careful angular correction** should be considered in future retrievals to improve the overall quality of the level-1b data.

In conclusion, the developed algorithm provides promising quality under cloud free and stationary conditions over most surface types from tropics to the mid-latitudes. The Ross-Li BRDF model describes the surface accurately and shows promising results over bright surfaces.

To further improve the algorithm, the polarization channels of POLDER shall be taken into account to enhance the information content available to the algorithm. By introducing polarization, the algorithm can take advantage of the property that cirrus clouds exhibit their own polarized signature [50], leading to improved cloud masking. The polarized data can be also utilized for retrieving aerosol above clouds and characterizing the aerosol and the cloud layers by exploiting the sensitivity in polarized measurements [51].

References

[1] John M. Wallace and Peter V. Hobbs. *Atmospheric Science: An Introductory Survey*. Second Edition, INTERNATIONAL GEOPHYSICS SERIES, Vol.92 , 2005.

[2] Marco Vountas, Kristina Belinska, Vladimir V. Rozanov, Luca Lelli, Linlu Mei, Soheila Jafariserajehlou, John P. Burrows. *Retrieval of aerosol optical thickness and surface parameters based on multi-spectral and multi-viewing space-borne measurements*. Journal of Quantitative Spectroscopy and Radiative Transfer, Volume 256, November, 2020.

[3] Coddington, O.; Lean, J. L.; Pilewskie, P.; Snow, M.; Lindholm, D. *"A Solar Irradiance Climate Data Record"*. Bulletin of the American Meteorological Society. 97 (7): 1265–1282, 2016, doi:10.1175/bams-d-14-00265.1

[4] K. N. Liou. *An Introduction to Atmospheric Radiation*. INTERNATIONAL GEOPHYSICS SERIES, Second Edition, Vol. 84, 2002

[5] M. L. Salby. *Fundamentals of Atmospheric Physics*. International Geophysics Series, Academic Press, USA, 1996.

[6] Hecht, Eugene. *Optics, Fourth Edition*. Boston: Addison-Wesley Publishing, 2001.

[7] J A Coakley. *REFLECTANCE AND ALBEDO, SURFACE*. Elsevier Science Ltd, 2003

[8] K. J. Ranson, J. R. Irons, and C. S. T. Daughtry. *Surface Albedo from Bidirectional Reflectance*. REMOTE SENS. ENVIRON. 35:201-211 (1991).

[9] Charles K. Gatebe, Michael D. King, Steve Platnick, G. Thomas Arnold, Eric F. Vermote, and Beat Schmid. *Airborne spectral measurements of surface–atmosphere anisotropy for several surfaces and ecosystems over southern Africa*. JGR Atmpspheres, American Geophysical Union, March 2003.

[10] Charles K.Gatebe, and Michael D.King. *Airborne spectral BRDF of various surface types (ocean, vegetation, snow, desert, wetlands, cloud decks, smoke layers) for remote sensing applications*. REMOTE SENS. ENVIRON. Vol. 179, pages 131:148, June, 2016.

[11] Pierre-Yves Deschamps, FranCois-Marie Brdon, Marc Leroy, Alain Podaire, Annick Bricaud, Jean-Claude Buriez, and Genevikve Skze. *The POLDER Mission: Instrument Characteristics and Scientific Objectives*. IEEE TRANSACTIONS ON GEOSCIENCE AND REMOTE SENSING, VOL. 32, NO. 3, MAY 1994.

[12] F.-M. Bréon (CEA/LSCE) with With help from the CNES Parasol team. *Parasol Level-1 Product Data Format and User Manual*. Ed. 1 - Rev. 4, Dec 13 , 2016.

[13] AERONET: System Description. `https://aeronet.gsfc.nasa.gov/new_web/system_descriptions.html`

[14] William Emery and Adriano Camps. *Introduction to Satellite Remote Sensing, Atmosphere, Ocean, Cryosphere and Land Applications*. Elsevier, 2017, DOI: 10.1016/C2015-0-04517-8.

[15] Coddington, O.; Lean, J. L.; Pilewskie, P.; Snow, M.; Lindholm, D. *"A Solar Irradiance Climate Data Record"*. Bulletin of the American Meteorological Society. 97 (7): 1265–1282, 2016, doi:10.1175/bams-d-14-00265.1

[16] Francois-Marie and Stephane Colzy *"Cloud Detection from the Spaceborne POLDER Instrument and Validation against Surface Synoptic Observations"*. American Meterological Society Journal, June 1999.

[17] A. Smirnov, B. N. Holben, T. F. Eck, O. Dubovik, and I. Slutsker *"Cloud-Screening and Quality Control Algorithms for the AERONET Database"*.Remote Sensing of Environment, Volume 73, Issue 3, 2000, Pages 337-349, ISSN 0034-4257.

[18] Liam Gumley, Jacques Descloitres and Jeffrey Schmaltz *"Creating Reprojected True Color MODIS Images: A Tutorial"*. Version 1.0.2, 14 January 2010

[19] Steven Platnick et al, *"MODIS Cloud Optical Properties: User Guide for the Collection 6/6.1 Level-2 MOD06/MYD06 Product and Associated Level-3 Datasets"*. Version 1.1. July, 2018

[20] Damien Sulla-Menashe and Mark A Friedl *"User Guide to Collection 6 MODIS Land Cover (MCD12Q1 and MCD12C1) Product"*. May 14, 2018

[21] V.V. Rozanov, A.V. Rozanov, A.A. Kokhanovsky, and J.P. Burrows *Radiative transfer through terrestrial atmosphere and ocean: Software package SCIATRAN*. Journal of Quantitative Spectroscopy and Radiative Transfer, 2014.

[22] Gao, F., Schaaf, C.B., Strahler, A.H., Jin, Y., Li, X. *Detecting vegetation structure using a kernel-based BRDF model.*. Remote Sensing of Environment 86, 198–205, 2003.

[23] Roujean, J., Leroy, M., Deschamps, P. *A Bidirectional Reflectance Model of the Earth's Surface for the Correction of Remote Sensing Data*. Journal of Geophysical Research 97, 20,455–20,468, 1992.

[24] Mishchenko MI, Travis LD, Lacis AA. *Multiple scattering of light by particles*. Cambridge: University Press; 2006.

[25] Mishchenko MI, Dlugach JM, Yanovitskij EG, Zakharova NT *Bidirectional reflectance of flat, optically thick particulate layers: an efficient radiative transfer solution and applications to snow and soil surfaces*. Journal of Quantitative Spectroscopy Radiative Transfer 1999;63:409–32

[26] Kneizys FX, Shettle EP, Abreu LW, Chetwynd JH, Anderson GP, Gallery WO, et al *Users Guide to LOWTRAN 7. Technical Report. Environmental research papers*. No. 1010, Air Force Geophysics Laboratory; 1986

[27] Köpke P, Hess M. *Manual for database OPAC, Optical properties of aerosols and clouds*. Meteorologisches Institute der Universität München; 1994

[28] Sinnhuber B-M, Sheode N, Sinnhuber M, Chipperfield MP, Feng W. *The contribution of anthropogenic bromine emissions to past stratospheric ozone trends: a modelling study*. Atmospheric Chemistry and Physics 2009;9:2863–71

[29] Bruhl C, Crutzen PJ. *MPIC two-dimensional model. In The atmospheric effects of stratospheric aircraft*. NASA Reference Publication 1993;1292:103–4.

[30] *Committee on Extension to the Standard Atmosphere. Washington, DC*. U.S. Standard Atmosphere, 1976, Government Printing Office; 1976.

[31] Rothman LS, Gordon IE, Barbe A, ChrisBenner D, Bernath PF, Birk M, et al. *The HITRAN 2008 molecular spectroscopic database*. Journal of Quantitative Spectroscopy Radiative Transfer 2009;110:533–72

[32] Lenoble J, editor. *Radiative transfer in scattering and absorbing atmospheres*. Hampton, VA, USA: A. Deepak Publishing; 1985.

[33] F. Maignana, F.-M. Bréon, R. Lacaze. *Bidirectional reflectance of Earth targets: Evaluation of analytical models using a large set of spaceborne measurements with emphasis on the Hot Spot*. Remote Sensing of Environment 90 (2004) 210–220

[34] Kristina Belinska *Aerosol property retrieval using multiviewing spaceborne POLDER measurements*. Master thesis. University of Bremen, 2019.

[35] K. D. Knobelspiesse, B. Cairns, B. Schmid, M. O. Roman, and C. B. Schaaf. *Surface BRDF estimation from an aircraft compared to MODIS and ground estimates at the Southern Great Plains site*. Journal of Geophysical Research, 113, 2008.

[36] Oleg Dubovik and Michael D. King *A flexible inversion algorithm for retrieval of aerosol optical properties from Sun and sky radiance measurements*. Journal of Geophysical Research Atmospheres 105696(27):673-20. August, 2000.

[37] T. Nakajima, M. Tanaka, T. Yamauchi *Retrieval of the optical properties of aerosols from aureole and extinction data*. Applied Optics, 22 (1983), pp. 2951-2959

[38] Bates DR. *Rayleigh scattering by air*. Planetary and Space Science. 1984;32(6): 785–90.

[39] Bucholtz A. *Rayleigh-scattering calculations for the terrestrial atmosphere*. Applied Optics 1995;34(15):2765–73.

[40] Bodhaine BA, Wood NB, Dutton EG, Slusser JR. *On Rayleigh optical depth calculations*. Journal of Atmospheric and Oceanic Technology, 1999;16:1854–61.

[41] Levy, R.C., Remer, L.A., Dubovik, O. *Global aerosol optical properties and application to moderate resolution imaging spectrora-diometer aerosol retrieval over land*. Journal of Geophysical Research: Atmospheres 112. DOI:10.1029/2006JD007815.

[42] Gorshelev, V., Serdyuchenko, A., Weber, M., Chehade, W., Burrows, J.P. *High spectral resolution ozone absorption cross-section Part 181: Measurements, data analysis and comparison with previous mea- surements around 293 K.*. Atmospheric Measurement Techniques 7, 609–624, 2014.

[43] Bogumil, K., Orphal, J., Homann, T., Voigt, S., Spietz, P., Fleis-chmann, O., Vogel, A., Hartmann, M., Kromminga, H., Bovensmann, H., Frerick, J., Burrows, J. *Measurements of molecular ab- sorption spectra with the sciamachy pre-flight model: instrument characterization and reference data for atmospheric remote-sensing in the 230–2380 nm region*. Journal of Photochemistry and Photobiology A: Chemistry 157, 167 – 184. Atmospheric Photochemistry, 2003.

[44] Geoffrey William McCamley. *Characterising Vegetation Structure Using MODIS Multi-Angular Data*. PhD thesis, RMIT University. January, 2014.

[45] A. Kokhanovsky. *Optical properties of terrestrial clouds*. Earth-Science Reviews 64 (2004) 189–241.

[46] L. A. Remer et al., *The MODIS Aerosol Algorithm, Products, and Validation*. Journal of the Atmospheric Sciences. Volume 62: Issue 4.

[47] Christine ERIKSEN *Why do they burn the 'bush'? Fire, rural livelihoods, and conservation in Zambia*. The Geographical Journal, Vol.173, No. 3, September 2007, pp. 242–256.

[48] Fabien Waquet et al,. *Global analysis of aerosol properties above clouds*. November 2013. Geophysical Research Letters 40(21):5809-5814.

[49] Sunita Verma, Divya Prakash, Manish Soni and Kirpa Ram. *Atmospheric Aerosols Monitoring: Ground and Satellite-Based Instruments*. Advances in Environmental Monitoring and Assessment, 2019.

[50] Goloub P, Herman M, Parol F. *Polarization of Clouds*. Proc. SPIE 2582, Atmospheric Sensing and Modeling II, (15 December 1995); doi: 10.1117/12.228551

[51] F. Peers et al., *Absorption of aerosols above clouds from POLDER/PARASOL measurements and estimation of their direct radiative effect*. Atmos. Chem. Phys., 15, 4179–4196, 2015 https://doi.org/10.5194/acp-15-4179-2015

Appendices

A Barrow station

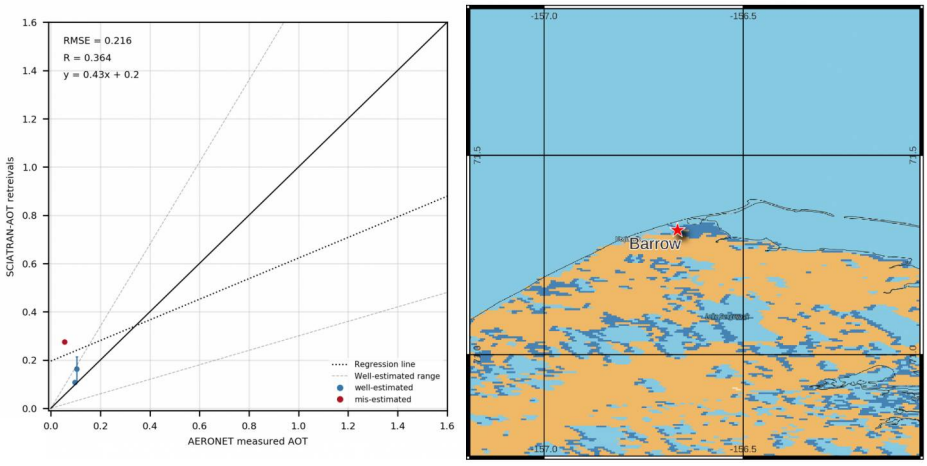

Figure 37: Left: Scatter plot of extracted days, Right: Land cover type of Barrow station surrounding environment

Barrow			
Land Cover and Environment: Grassland/Snow/Wetlands			
Date	SCIATRAN	POLDER CM	Notes
20	Over	Clear	Only one pixel colocated !!
22	Well	Clear	Few pixels are colocated
23	Well	Clear	Few pixels are colocated

Table 12: Retrieval evaluation of 3 extracted days in August 2008 at Barrow station. Rejected retrievals are colored in gray

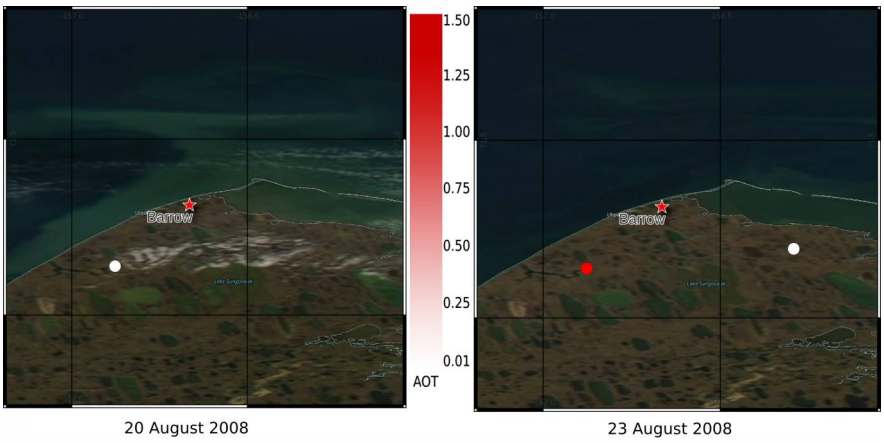

Figure 38: MODIS true color images for Barrow station.

B Egbert station

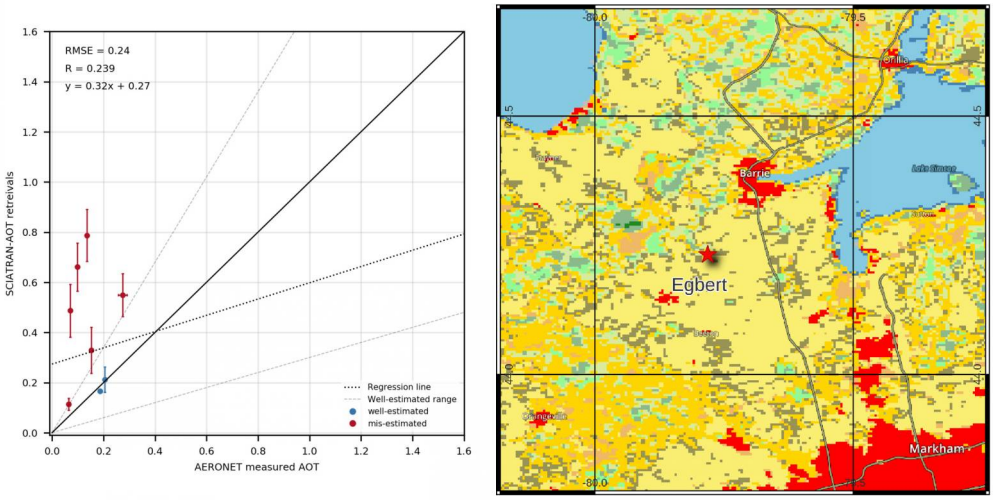

Figure 39: Left: Scatter plot of extracted days, Right: Land cover type of Egbert station surrounding environment

Egbert			
Land Cover and Environment: Cropsland/Vegetation			
Date	SCIATRAN	POLDER CM	Notes
06	Over	Good	Low and patchy clouds
08	Over	Poor	Cloudy Scene
11	Well	Fair	NONE
17	Over	Poor	Cloudy scene
18	Over	Poor	Cloudy scene
20	Well	Clear	NONE
24	Over	Poor	Thin clouds
31	Over	Good	Few pixels remain after applying constraints

Table 13: Retrieval evaluation of 8 extracted days in August 2008 at Egbert station. Rejected retrievals are colored in gray

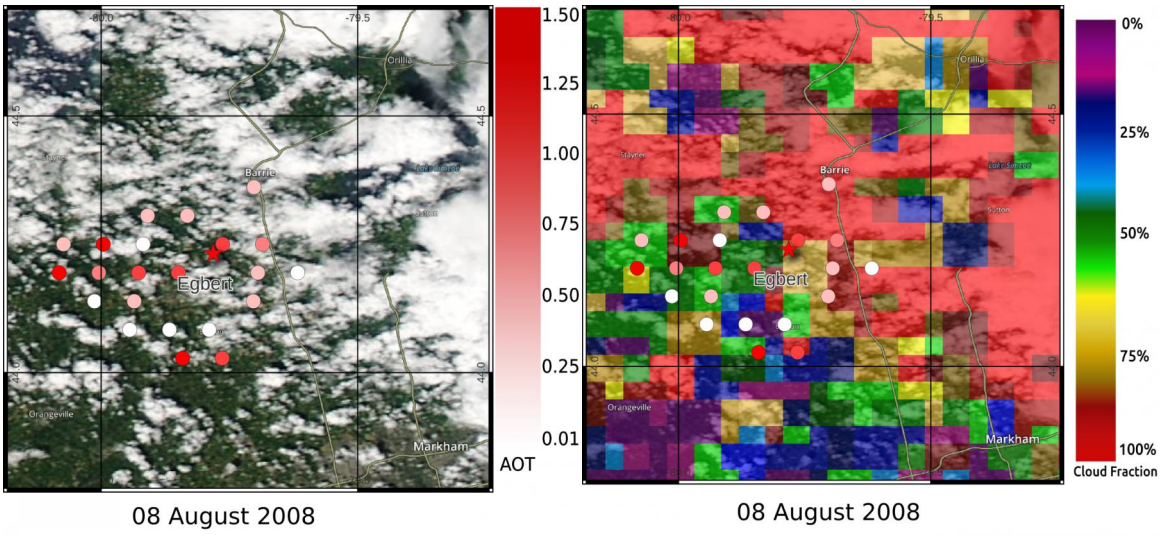

Figure 40: Retrieved AOT over Egbert AERONET station. Left Column: MODIS true color images. Right Column: color coded MODIS cloud fraction values

C Ji Parana SE station

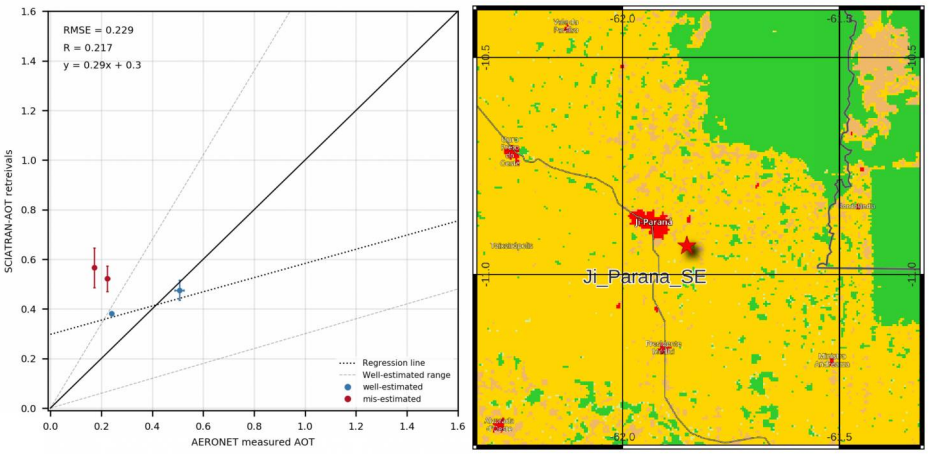

Figure 41: Left: Scatter plot of extracted days, Right: Land cover type of Ji Parana SE surrounding environment

Ji_Parana			
Land Cover and Environment: Savannas			
Date	SCIATRAN	POLDER CM	Notes
08	Over	Good	Low and patchy clouds
10	Over	Fair	Low and patchy clouds
15	Well	Clear	NONE
17	Well	Good	NONE

Table 14: Retrieval evaluation of 4 extracted days in August 2008 at Ji Parana SE station. Rejected retrievals are colored in gray

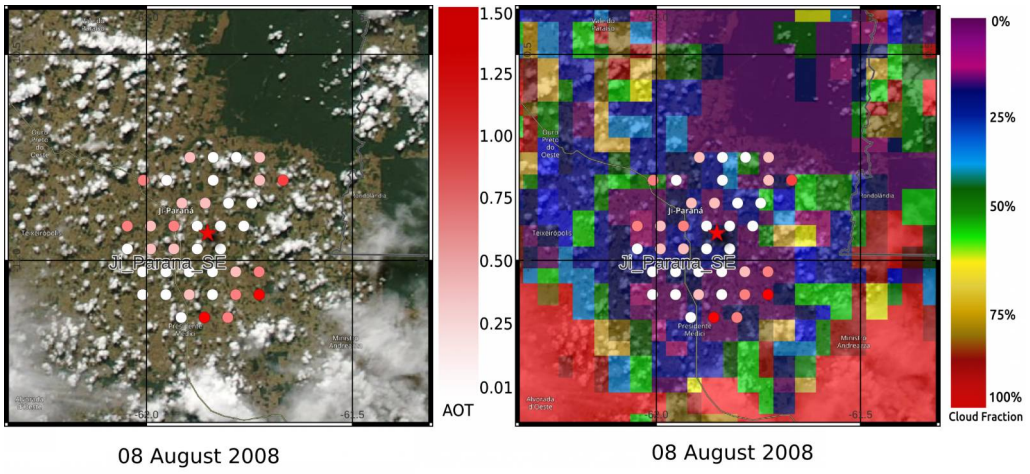

Figure 42: Retrieved AOT over Ji Parana SE AERONET station. Left Column: MODIS true color images. Right Column: color coded MODIS cloud fraction values

D Kanpur station

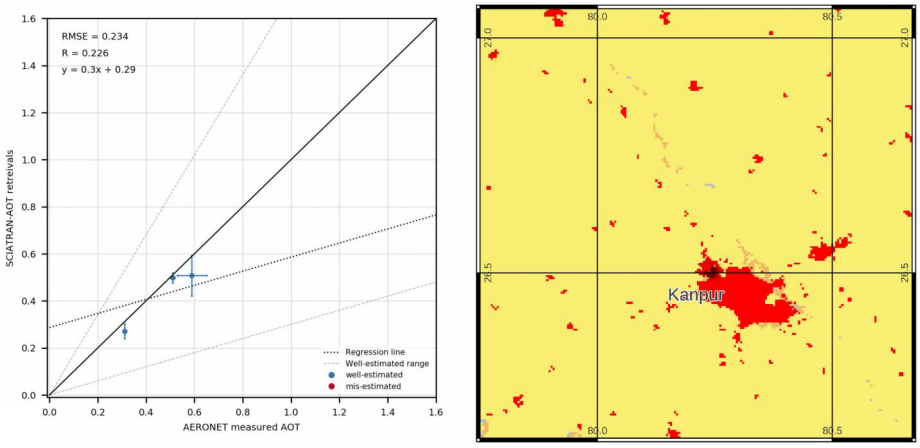

Figure 43: Left: Scatter plot of extracted days, Right: Land cover type of Kanpur station surrounding environment

Kanpur			
Land Cover and Environment: Urban/Cropsland			
Date	SCIATRAN	POLDER CM	Notes
24	Well	Poor	Probable aerosol over clouds
28	Well	Clear	NONE
30	Well	Good	NONE

Table 15: Retrieval evaluation of 3 extracted days in August 2008 at Kanpur station. Rejected retrievals are colored in gray

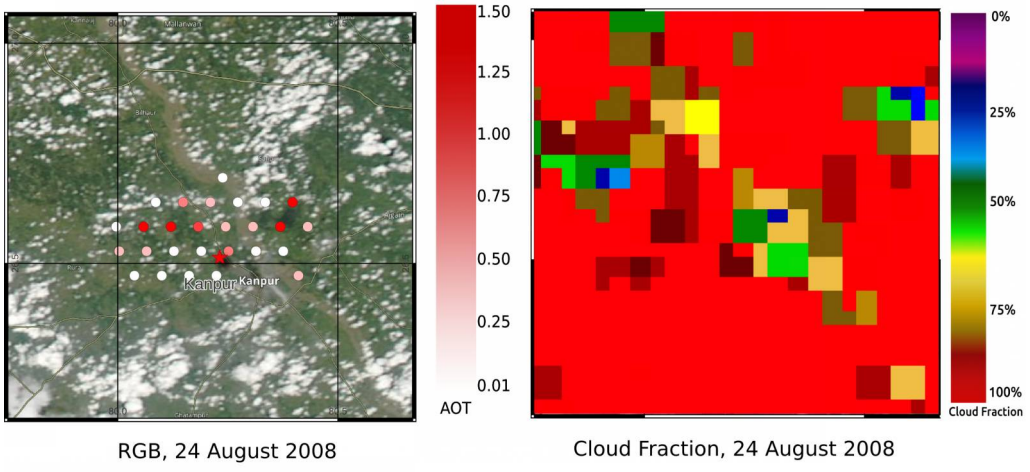

Figure 44: Retrieved AOT over Kanpur AERONET station. Left Column: MODIS true color images. Right Column: color coded MODIS cloud fraction values

E Karachi station

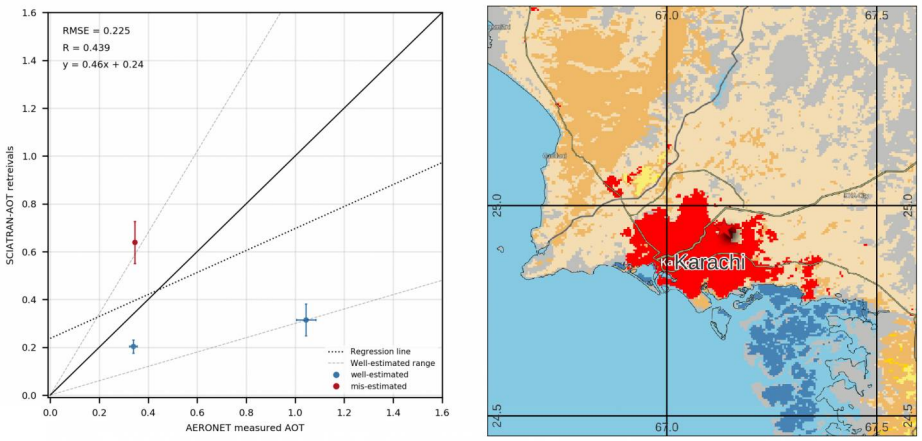

Figure 45: Left: Scatter plot of extracted days, Right: Land cover type of Karachi station surrounding environment

Karachi			
Land Cover and Environment: Urban/open Shrublands			
Date	SCIATRAN	POLDER CM	Notes
25	Well	Clear	NONE
27	Over	Fair	Low and patchy clouds, probable heavy load of aerosols.
31	Under	Good	Cloud mask has screened majority of pixels, few pixels remain, and probable aerosol over clouds.

Table 16: Retrieval evaluation of 3 extracted days in August 2008 at Karachi station. Rejected retrievals are colored in gray

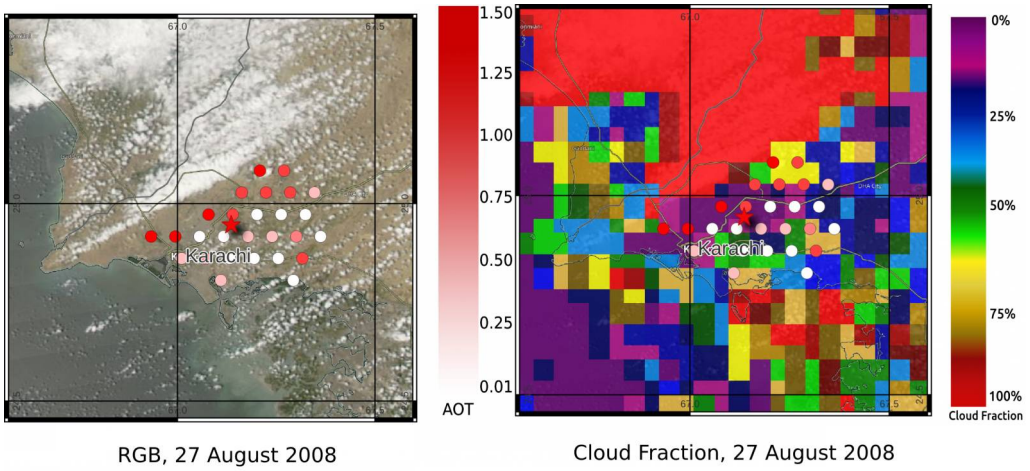

Figure 46: Retrieved AOT over Karachi AERONET station. Left Column: MODIS true color images. Right Column: color coded MODIS cloud fraction values

F Palaiseau station

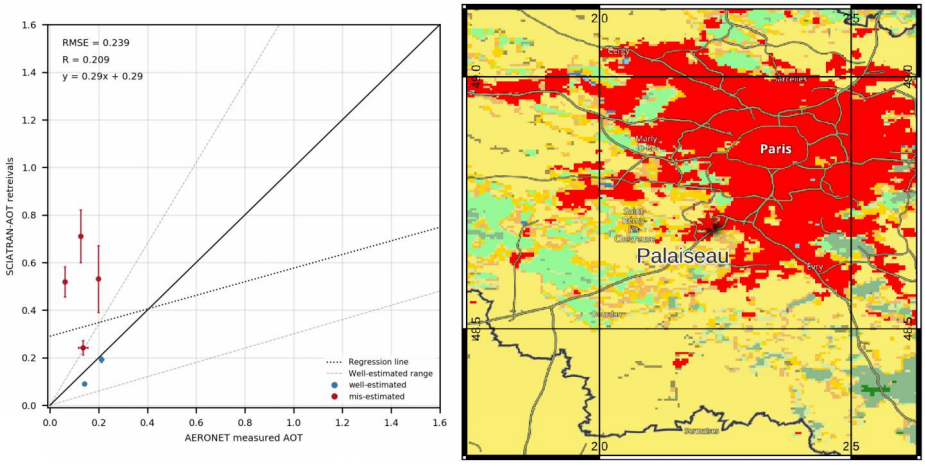

Figure 47: Left: Scatter plot of extracted days, Right: Land cover type of Palaiseau station surrounding environment

Palaiseau			
Land Cover and Environment: Urban/Croplands			
Date	SCIATRAN	POLDER CM	Notes
12	Over	Fair	Low and patchy clouds
19	Over	Poor	NONE
23	Over	Poor	NONE
25	Over	Good	At the the expected error limits
27	Well	Clear	NONE
30	Well	Clear	NONE

Table 17: Retrieval evaluation of 6 extracted days in August 2008 at Palaiseau station. Rejected retrievals are colored in gray

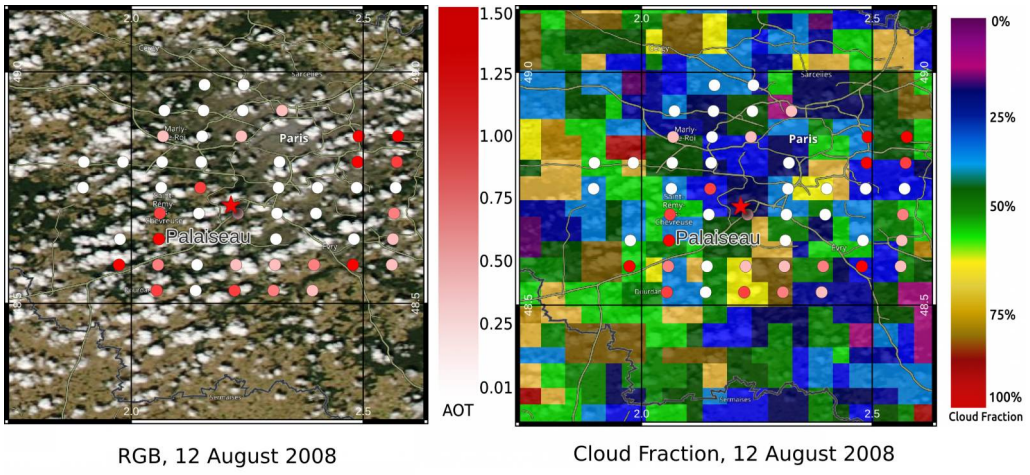

Figure 48: Retrieved AOT over Palaiseau AERONET station. Left Column: MODIS true color images. Right Column: color coded MODIS cloud fraction values

G Rio Branco station

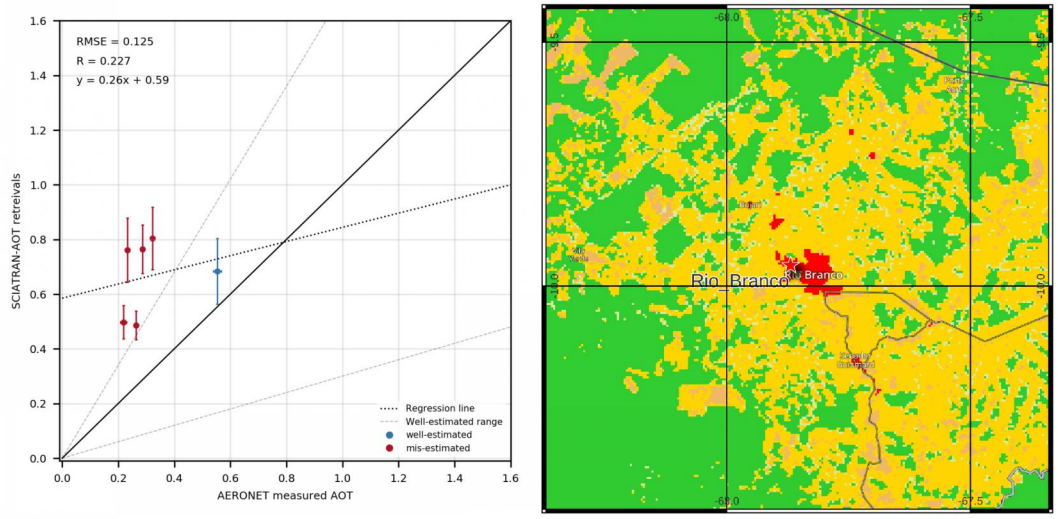

Figure 49: Left: Scatter plot of extracted days, Right: Land cover type of Rio Branco station surrounding environment

Rio Branco			
Land Cover and Environment: Urban/Savannas			
Date	SCIATRAN	POLDER CM	Notes
06	Over	Fair	Low and patchy Clouds
08	Over	Fair	Low and patchy Clouds
11	Over	Poor	Low and patchy Clouds
15	Over	Fair	Low and patchy Clouds
17	Over	Fair	Low and patchy Clouds
20	Well	Poor	Applying the constraints removed majority of cloudy pixels

Table 18: Retrieval evaluation of 6 extracted days in August 2008 at Rio Branco station. Rejected retrievals are colored in gray

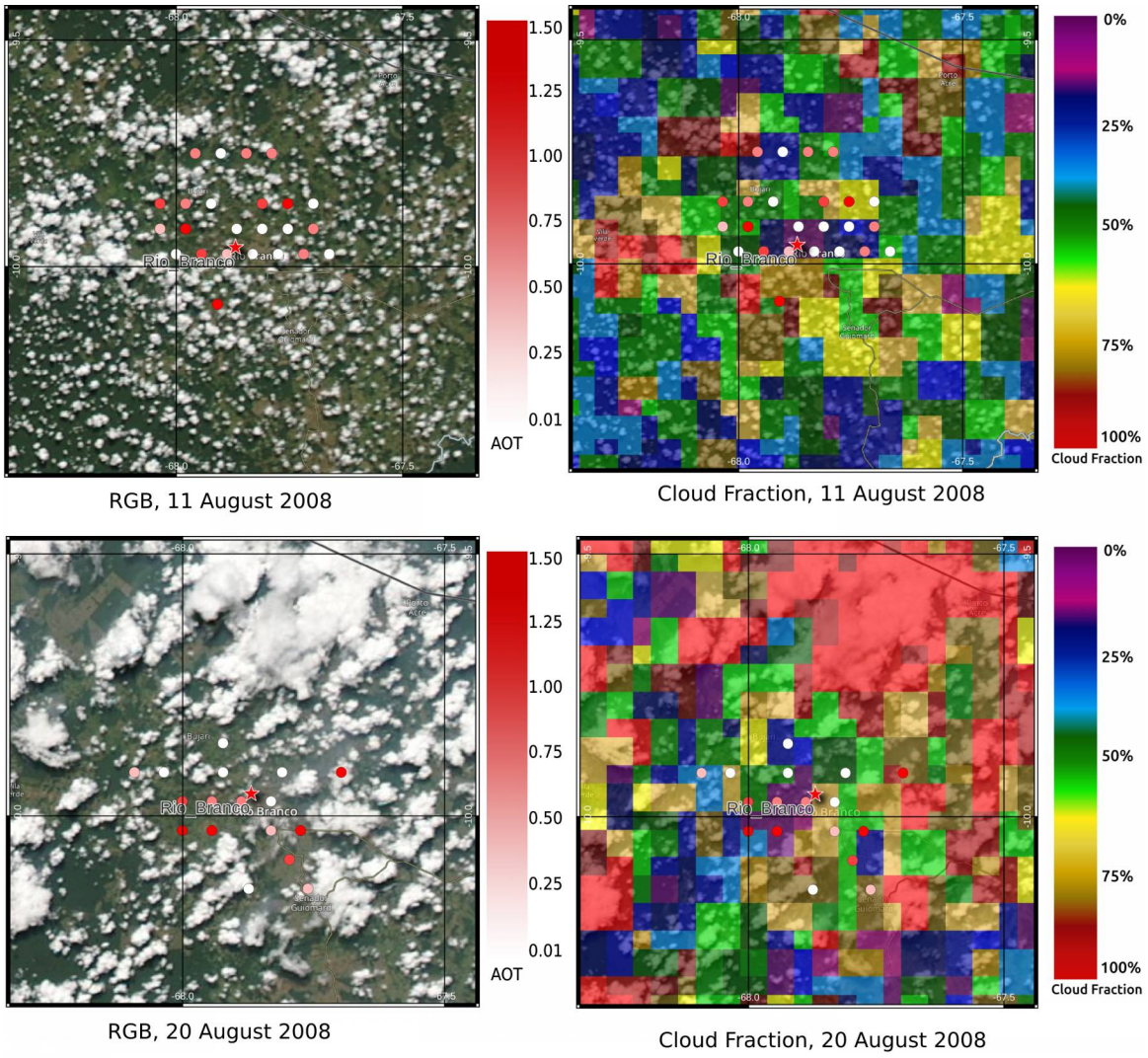

Figure 50: Retrieved AOT over Rio Branco AERONET station. Left Column: MODIS true color images. Right Column: color coded MODIS cloud fraction values

H SACOL station

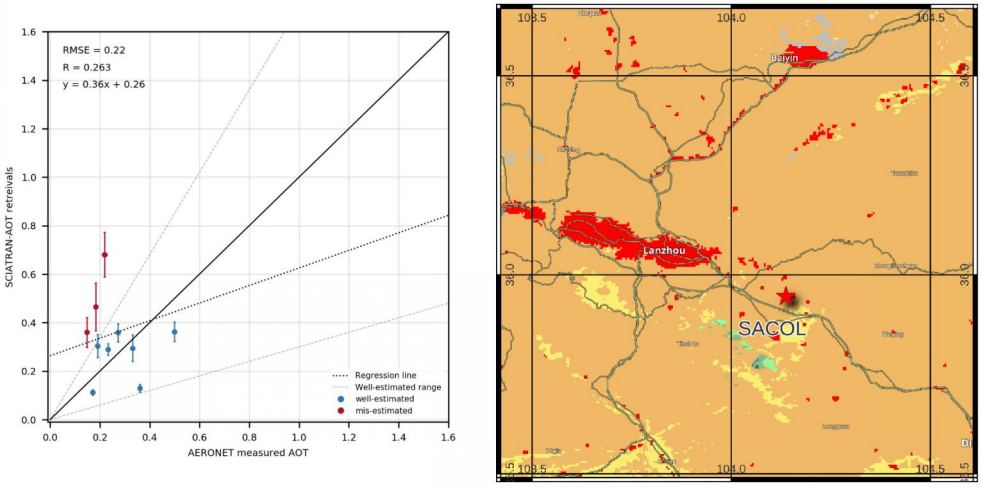

Figure 51: Left: Scatter plot of extracted days, Right: Land cover type of SACOL station surrounding environment

SACOL			
Land Cover and Environment: Grasslands			
Date	SCIATRAN	POLDER CM	Notes
09	Over	Good	Heavy aerosol load from Lanzhou city, wind direction fitting with rapidly changing conditions (wunderground.com)
10	Well	Fair	NONE
12	Over	Fair	Thin Clouds in the scene, Heavy load from Lanzhou city
14	Well	Clear	NONE
16	Well	Clear	NONE
17	Well	Clear	NONE
19	Well	Fair	NONE
21	Well	Clear	NONE
25	Well	Clear	NONE
30	Over	Fair	Thin clouds in the scene

Table 19: Retrieval evaluation of 10 extracted days in August 2008 at SACOL station. Rejected retrievals are colored in gray

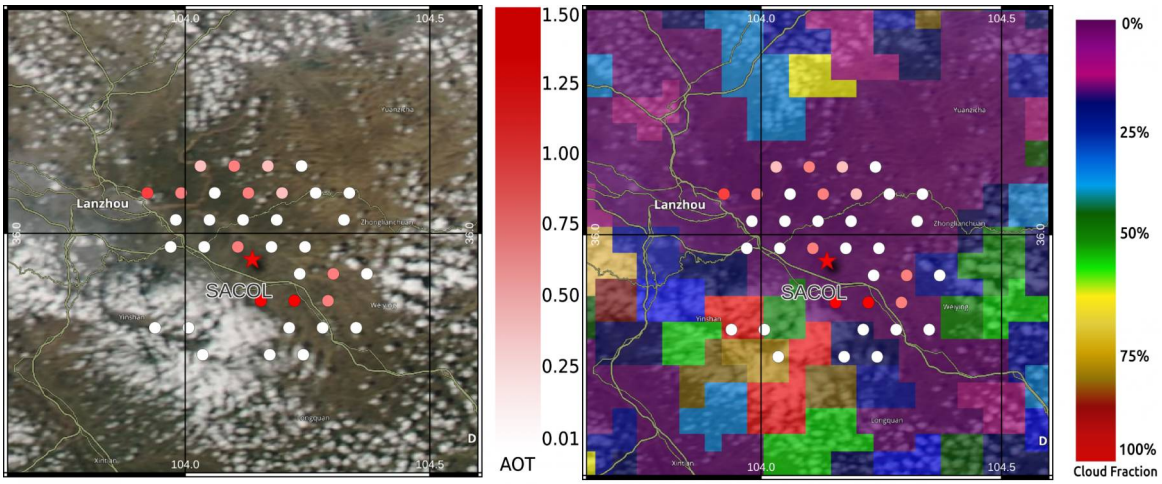

Figure 52: Retrieved AOT over SACOL AERONET station. Left Column: MODIS true color images. Right Column: color coded MODIS cloud fraction values